C.P. No. 1269

C.P. No. 1269

PROCUREMENT EXECUTIVE, MINISTRY OF DEFENCE

AERONAUTICAL RESEARCH COUNCIL
CURRENT PAPERS

The External Drag of Fuselage Side Intakes: Rectangular Intakes with Compression Surfaces Vertical

by

M. D. Dobson

Aerodynamics Dept., R.A.E., Bedford

LONDON: HER MAJESTY'S STATIONERY OFFICE
1974
PRICE *£1.25* NET

UDC 533.697.24 : 533.6.013.12 : 533.6.013.122

CP No.1269 *
October 1972

THE EXTERNAL DRAG OF FUSELAGE SIDE INTAKES: RECTANGULAR INTAKES WITH COMPRESSION SURFACES VERTICAL

by

M. D. Dobson

SUMMARY

An experiment designed to measure the external drag of fuselage side intakes is described. The scope of the experiment and the techniques employed are discussed and an assessment is made of the accuracy of results.

Measurements of the external drag of rectangular intakes installed on the sides of a fuselage are presented. Results at subsonic speeds show that drag at full flow is independent of compression surface geometry, so that substantial flow spillage may be achieved for little drag penalty provided that the intake throat Mach number is kept high by elevation of the compression surface. For a given total turning of the flow by the compression surface, spillage drag is found to be uniquely related to the inlet mass flow ratio (as distinct from capture mass flow ratio). Radius of the cowl lip is found to affect the drag of the intake at full flow but becomes less important as flow is reduced. Drag at full flow for intakes with swept end walls is lower than for a configuration in which they are unswept but the spillage drag rise is greater.

At supersonic speeds the variation in full flow drag with compression surface geometry may be predicted from consideration of the changes in shock geometry but there is generally a small positive increment which is not accounted for in the calculation. Calculation methods based on theoretical shock geometry are found to over estimate spillage drag.

---

* Replaces RAE Technical Report 72202 - ARC 34455

CONTENTS

1 INTRODUCTION

Engines of the current generation of designs for multi-mission combat aircraft are generally contained within the fuselage. They are fed with air by intakes located in the sides and exhaust *via* nozzles at or upstream of the end of the fuselage. The correct representation of intake and exhaust flows and the simultaneous measurement of external forces poses one of the major problems of wind-tunnel testing and at present the only satisfactory way of obtaining accurate measurements, particularly of drag, is to study the effects of intake or exhaust flow representation on partial models that do not fully represent the complete aircraft.

A partial model has been designed which allows the drag to be measured of representative configurations of twin intakes mounted on the sides of a fuselage at both subsonic and supersonic speeds. The technique used is that of mounting the complete model of fuselage and intakes on a balance, 'earthing' the intake flow control valves and subtracting measured internal and base drags from the total force measurement to obtain external drag.

In the design of the experimental arrangement, care has been taken to:-

(a) ensure that the necessary accuracy can be achieved in the measurement of drag to allow adequate assessment of small drag increments associated with flow spillage, changes of intake detail design etc. and

(b) obtain flexibility of configuration which may be tested, i.e. the type of intake, its position on the fuselage and its detail design.

To the present time several configurations of intake have been tested with this arrangement, using the same fuselage for all tests and a resumé of results obtained was presented in Ref.1. Results used in this reference included some data obtained with the present rectangular intake and the present Report, as well as introducing some new data, also re-presents the conclusions of Ref.1. However the data used here to support these conclusions are, in most cases, obtained from other configurations of the intake so that the data contained in this reference are not precisely duplicated. Thus the present Report confirms the conclusions of Ref.1 using, in most cases, the evidence of similar but not identical test configurations.

The techniques used in this experiment are dealt with at some length here and its overall accuracy is discussed. These techniques apply equally to all intakes in the series and are not specific to the particular rectangular configuration discussed here.

2 EXPERIMENTAL TECHNIQUE

2.1 Model

A photograph of an 'exploded' model similar* to that used in the present experiments is shown in Fig.1. It consists of a forward fuselage constructed in the form of a fork in which the two prongs form dorsal and ventral spines along the length of the model. A nose and canopy fit onto this fork and the whole is supported on a sting which incorporates a five-component strain gauge balance. Sides carrying the diverters and intake nacelles, secured between the spines of the fuselage, complete the model. A simple wedge diverter is used for the removal of the fuselage boundary layer and the fuselage sides have been made flat in the region of the intake so that the depth of the diverter remains constant over the width of the intake. This is illustrated in Fig.2a. The intakes (nacelles) may be removed from the fuselage and replaced by flat sides, Fig.2b, to give a 'clean' fuselage configuration. Variations in intake geometry are effected by making the cowls, compression surfaces, compression surface fairings and diverter wedges detachable. The depth of the diverter may be varied by adjusting the entire nacelle laterally with respect to the fuselage. This is done by sliding it between the parallel surfaces of the fuselage spines.

2.2 Measurements

Three components of drag are measured which are combined to give the total external drag coefficient of the model, C_{D_E}, where:-

$$C_{D_E} = \frac{D_E}{q_\infty 2A_e} = C_{D_{bal}} - C_{D_{base}} - 2C_{D_I} \qquad (1)$$

in which A_e = entry area

$C_{D_{bal}}$ = drag coefficient measured by the balance

---

* The intake design shown in this photograph is actually of a half axi-symmetric type. However the assembly of the present configuration (shown in Fig.2a) is similar.

$C_{D_{base}}$ = base drag coefficient

$2C_{D_I}$ = sum of the measured internal drag coefficient of the two ducts.

Net overall drag of the model is obtained using a strain-gauge balance which measures normal, side and axial forces and pitching and yawing moments. Although components other than axial force are of interest in their own right, their measurement is necessary to provide an accurate assessment of axial force because of balance interactions.

Base drag is measured using an array of forward-facing pressure tubes, three of which may be seen in Fig.2c. These tubes are secured to the sting and positioned close to the model base and incorporate an electrical device which warns of any contact between them and the model. Distribution of base pressure has been examined for a range of test conditions and individual base pressure tubes are located to give increased coverage in regions where pressure gradients occur*. The pressure measured by each tube is area weighted accordingly in the calculation of base drag. The peripheries of the base of the model and the duct exits have been shrouded, Fig.2c, in an attempt to improve the uniformity of base pressure but no verification of the efficiency of this technique has yet been made.

Internal flow is controlled and measured by instrumentation which is supported directly by the sting and therefore the drag associated with it does not appear in the internal drag summation. Type B mass flow units[2] are used, one of which is shown schematically in Fig.3. It consists of a square-section box which contains the driving mechanisms and position indicators for the translating exit plug which controls the flow and the rotating pressure rake which measures the flow. The box is supported by brackets from the sting and the exit plug and pressure rake are cantilevered forward into the duct. The supporting brackets include adjusting arrangements whereby the mass flow unit may be aligned with the duct exit which is 'floating' because of the flexible balance. The pressure rake carries twelve pitot tubes across a diameter and two static probes, one located centrally and the other at about 0.75 duct radius. The layout of these pressure tubes is shown in Fig.3. Pitot tubes are

---

* Base pressure is found to be least uniform in regions where the internal and external flows are in closest proximity but in these regions the local base areas are small.

located so that they survey nominally equal areas of the duct but because of the necessity to maintain adequate clearance between the outer tubes and the floating duct wall, the outer tubes depart from this equal area distribution. These outer tubes of the rake carry an electrical device which warns of any contact with the model. The plane of the duct which the instrumentation surveys is upstream of the spool on which the pressure tubes are carried so that the drag of the spool is not measured. Also, this plane is located upstream of the exit and therefore the instrumentation does not measure the skin friction drag on the parallel duct wall between these stations. This quantity is calculated for each internal flow condition, using skin friction data for flat plates[3].

2.3 Calculation of internal drag

Referring to Fig.4, the general expression for the standard internal drag[4] from a station at ∞ upstream to the duct measuring station f is:-

$$D_I = \rho_\infty V_\infty^2 A_\infty - \left[(p_f - p_\infty)\cos\phi + \rho_f V_f^2 \cos\psi \cos\theta\right] A_f \quad . \qquad (2)$$

For the present model, duct incidence (θ) remained zero and as $\psi = \phi = 0^o$ the expression reduces to:-

$$D_I = \rho_\infty V_\infty^2 A_\infty - \left[p_f - p_\infty + \rho_f V_f^2\right] A_f \qquad (3)$$

whence, non-dimensionalising by $q_\infty A_e$ and putting:-

$$\rho_\infty V_\infty^2 = 2q_\infty$$

and

$$\rho_f V_f^2 = \gamma p_f M_f^2$$

we obtain the internal drag coefficient:-

$$C_{D_I} = \frac{2A_\infty}{A_e} - \frac{1}{q_\infty}\frac{A_f}{A_e}\left[(p_f - p_\infty) - \gamma p_f M_f^2\right] \qquad (4)$$

which is the form of the equation used in the present evaluation.

In order to obtain the required accuracy of measurement of internal mass flow, the duct and its instrumentation have been calibrated by the method described in Ref.2. The experimental arrangement used for this calibration is shown diagrammatically in Fig.5. Briefly, the wind tunnel is used as a vacuum vessel into which air is sucked from atmosphere. This air passes through and is measued by a standard orifice plate, whose discharge coefficient is known, and then passed through the model duct and the quantity measured by the duct instrumentation. For this, the 'supersonic' part of the intake is removed and replaced by a bell-mouth of contraction ratio 4:1. Duct instrumentation allows the mass flow ratio to be measured in several different ways and for each, calibration produces a factor, defined as:-

$$\frac{\text{mass flow ratio measured by orifice plate}}{\text{mass flow ratio measured by duct instrumentation}}$$

by which measured duct mass flow ratio may be corrected.

Depending on the pressure ratio* across the duct exit the flow will be either unchoked or choked. With the exit unchoked, the duct mass flow is obtained from measurements of the mean total pressure and mean static pressure at station f. A calibration factor K_f (Ref.2) is applied to this calculation. With the exit choked, the duct mass flow is obtained from the product of the area weighted mean total pressure at f and the effective area of the choked exit. In this case the calibration factor is applied in the form of an exit discharge coefficient $C_{d(P_f)}$, in which

$$A_x(\text{effective}) = A_x(\text{geometric}) \times C_{d(P_f)} \quad .$$

Calculation of the geometric exit area for this arrangement is given in Appendix A of Ref.2 but an accurate knowledge of its value is not necessary provided that, for a given exit plug position, it is identical during both calibration and test.

The calibration has shown that for sharp-edged exits, the pressure ratio above which $C_{d(P_f)}$ remains constant (the pressure ratio above which the flow is choked) is of the order 2.8 to 3.0. For intake tests at a free-stream

---

* Pressure ratio defined as $\dfrac{\text{area weighted mean total pressure at station f}}{\text{ambient pressure downstream of the exit}}$.

Mach number, M_∞, of 1.4, assuming normal shock intake pressure recovery and a 3% duct loss, the pressure ratio P_f/p_∞ would be 2.96. Thus at values of M_∞ greater than 1.4 the duct exit is likely to be choked while at values of M_∞ less than 1.4 it may not be*. In the present tests data taken at supersonic Mach numbers (the lowest is $M_\infty = 1.41$) are computed using the factor $C_{d(P_f)}$ and data taken at subsonic Mach numbers the factor K_f.

2.4 Correction factor for duct momentum flux

To calculate internal drag it is necessary to evaluate the change of momentum in the internal flow between stations at infinity upstream and in the duct. This involves the integration of ρu^2 across the duct, this term being expressed in equation (4) by $\gamma p_f M_f^2$ where p_f and M_f are mean values of duct static pressure and Mach number.

The total mass flow in the duct is given by $\int \rho u dA$ while the mass flow measured in the experiment is obtained from summation of the mass flows measured at discrete points in the duct flow and given by $\sum_1^N w_i \rho_i u_i$, in which N is the number of discrete points, w_i is the area weighting factor (because individual tubes are not necessarily associated with similar areas) and ρ_i and u_i are local values of density and velocity at the measuring points. A correction factor K may therefore be defined for the measured mass flow where:-

$$K = \frac{1}{A} \int \rho u dA \bigg/ \sum_1^N w_i \rho_i u_i \quad . \tag{5}$$

If, because of the relatively low velocities in the duct, density changes are ignored this may be written as:-

$$K = \frac{1}{A} \int \left(\frac{u}{u_m}\right) dA \bigg/ \sum_1^N \frac{u_i}{u_m} w_i \tag{6}$$

where u_m is the local maximum velocity in the duct flow.

---

* The computer program examines pressure ratio and reveals an unchoked exit.

A correction factor K2 may be defined for the momentum flux, analogous to the factor K defined above for mass flow correction where:-

$$K2 = \frac{1}{A}\int \rho u^2 dA \Bigg/ \sum_{1}^{N} w_i \rho_i u_i^2 \qquad (7)$$

or again, ignoring density changes

$$K2 = \frac{1}{A}\int \left(\frac{u}{u_m}\right)^2 dA \Bigg/ \sum_{1}^{N} w_i \left(\frac{u_i}{u_m}\right)^2 \quad . \qquad (8)$$

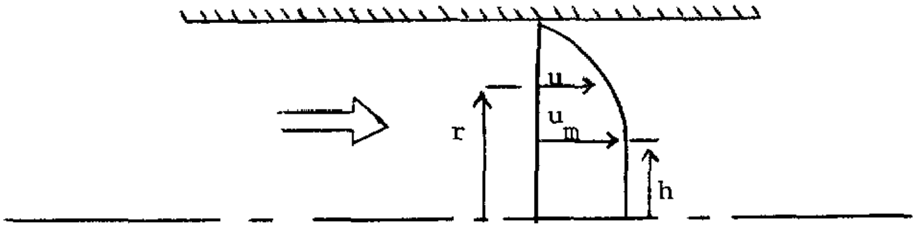

Referring to the sketch above, the flow cell may be considered as a duct of unit radius, in which the flow has a central core of uniform velocity of radius h and between this core and the duct wall a velocity profile with a turbulent boundary layer type of distribution i.e.

$$\frac{u}{u_m} = \left(\frac{1 - r}{1 - h}\right)^{1/n} \quad . \qquad (9)$$

The correction factors K and K2 have been computed for a family of such velocity distributions within the limits:-

$$2 \leqslant n \leqslant 8$$

and

$$0.2 \leqslant h \leqslant 0.8 \quad .$$

The factor K may be regarded as the theoretical counterpart of K_f, which is obtained from calibration. K_f is found to be a mild function of throttle position and over the range of throttle movement used in the experiment, the relationship between K and K2 may be approximated by a straight line, with a maximum deviation of about two-tenths of one percent for this family of velocity profiles. From this linear relationship correction factors for the momentum flux may be obtained using the correction factor for mass flow obtained from calibration, for each throttle position and provided that the velocity distribution found in the duct during experiment is within the family of profiles considered, the momentum flux will be correctly factored.

2.5 Assessment of accuracy

Equation (1) indicates that the external drag is obtained by subtracting base and internal drags from the balance drag. Each of these three components is large relative to the external drag and the sum of their individual accuracies will determine the net accuracy of external drag. To illustrate the relative magnitudes of the components of drag, Fig.6 shows the variation of the four coefficients with Mach number for conditions of full mass flow and about 20% spillage. Typically, at full mass flow at $M_\infty = 0.6$, $C_{D_{bal}} = 0.861$, $\left[C_{D_{base}} + C_{D_I}\right] = 0.609$ giving $C_{D_E} = 0.240$ (there is a small internal skin friction term of 0.012 as indicated in section 2.2). Spillage drag, defined as the difference in external drag between the value at full flow and that at 20% spillage, is approximately a C_{D_E} of 0.05 at $M_\infty = 0.6$ (Fig.6). A drag increment of 0.005 for say 2% spillage is less than one percent of the magnitude of the quantities required to obtain it and thus gives an idea of the accuracy required in the measurement of these quantities.

The overall accuracy of the measurement of external drag depends firstly on the instrumentation used for both force and pressure measurement and its associated calibration and secondly, the assessment of the area over which the pressure measured by a particular single pressure tube applies when the net force is obtained by integration of a number of pressure measurements. Considering the accuracies of the instrumentation and calibrations, Table 1 has been prepared to indicate the accuracy which might be expected in the component drag coefficients and hence in external drag for three test Mach numbers at values of A_∞/A_e used in Fig.6. The strain gauge balance was compensated for variations in ambient temperature and in both calibration and test was found generally to repeat to within ±0.2% of the range of the readout system. This is the standard used for the evaluation of the accuracy of the force data in

Table 1 and even if it is optimistic to some extent, it will be seen that balance error introduces only 10% of the total error. The manometers used for pressure measurement are calibrated to within ±34 N/m^2 and this is the standard used in the table. This may be a pessimistic standard as firstly, most of the manometers in use are known to be accurate to within half of the above value and secondly, net forces are obtained by integration of the values indicated by a number of instruments, which is likely to improve the 'net' instrument accuracy. However additional errors, not allowed for in the table, will be introduced by incorrect area weighting of the pressures used in the integrations. It is clear from the table that the main sources of error lie in the measurement of mass flow ratio, assumed to be accurate to ±0.003 and the measurement of the internal momentum flux which involves the accuracies of the factors K and K2. The measurement of these two quantities introduce about 60% of the estimated error in measurement of the absolute external drag coefficient.

With the intake operating in a supercritical condition at supersonic Mach numbers, variation of the throttle position will not affect the intake flow conditions and therefore both duct mass flow ratio and external drag should remain constant. This condition can therefore provide a useful indication of the scatter of results due to errors in measurement and some typical results are shown in Table 2. At each Mach number the mass flow remains constant to within 0.001 while the scatter in external drag coefficient of ±0.001 to ±0.004 is much less than the estimated values in Table 1. Table 3 presents some typical results obtained at subsonic speeds for a configuration in which the drag appears to remain constant over a small range of mass flow in the region of full intake flow. Assuming this to be so (though there is no aerodynamic reason why it should necessarily be true), the scatter of the results is seen to be similar to the supersonic values of Table 2.

With this model it is possible to alter the intake duct exit size by sleeving the duct from a point upstream of the internal measuring station to the exit. At $M_\infty = 2.0$ a particular model configuration was tested both with and without the ducts sleeved and results are shown in Fig.7. Each of these duct configurations was calibrated against a standard orifice plate and so the accuracy of mass flow measurement, ±0.003, applies to both. The maximum mass flows measured for the two cases are similar to within 0.001 which verifies the comparative accuracy of calibration. There appears to be some differences in measured external drag at high mass flow, where points for the sleeved duct are some 0.012 below points for the other configuration. Elsewhere within the mass flow range the maximum differences in external drag are about 0.006. It should be noted that the data presented in Tables 2 and 3 and Fig.7 are not necessarily for the present rectangular intake configuration but have been selected because of their relevance to the discussion.

From this assessment it is concluded that the accuracy in the measurement of increments in external drag coefficient is of the order ±0.005, which is of similar magnitude to the minimum drag increments which are required to be measured. The measurement of these increments (i.e. changes in drag due to changes in mass flow ratio, intake design, diverter position etc.) is the prime concern of this experiment. The achieved accuracy is considerably better than that estimated from consideration of the calibration and instrumentation accuracies but this defines the absolute accuracy of measurement of external drag coefficient, which is not of such great concern for this partial model.

3 TESTS

3.1 Intake configurations

Two rectangular intake configurations were tested, details of which are shown diagrammatically in sketches (a) and (b) of Fig.8. Intake 1 is a double wedge intake designed for the first oblique shock to fall on the cowl lip at a Mach number of 2.41. The angle of the first ramp is fixed at 10° while the second may be altered to one of the four discrete values shown in Fig.8a, by using interchangeable blocks, an appropriate third (subsonic diffuser) ramp (Fig.8a) is used in each case. Intake 2 (Fig.8b) has a single 10° wedge compression surface designed for the oblique shock to fall on the cowl lip at a Mach number of 2.00. Both of these intake configurations were oriented so that the undersides of their compression surfaces were adjacent to the sides of the fuselage.

Three cowls were available to be used with either intake configurations 1 or 2, the essential difference between them being the lip radius. Cowl A provided an intake with a sharp lip, cowl C an intake with a blunt lip and cowl B, one in between. Lip radius as a fraction of inlet height is given in Fig.8c. For this family of cowls the lip thickness is obtained by providing each with a similar internal profile and increasing the thickness externally. Increasing lip radius (lip bluntness) in this way produces an increase in 'highlight' height h_h of the cowl (see Fig.8c) and hence an increase in the highlight capture area of the intake. The slope of the surface, η_{ext} at the point z (see Fig.8c) is similar for all three cowls as is the non-dimensional longitudinal profile downstream of this point. Ordinates for this profile are given in Table 4. All three cowls faired into the same section at a station 1.43 h_e downstream of the inlet plane. In side elevation the inlet plane was canted down $2\frac{1}{2}^o$ relative to a vertical normal to the horizontal fuselage datum. Two endwall* configurations were available. In one the leading edges were in a spanwise direction and had lip radii similar to the cowl, thickness again being increased externally. In the other configuration, endwall leading edges were swept along lines from the compression surface leading edge to the cowl lip. These endwalls had sharp leading edges with parallel internal surfaces separated by a distance equal to w_e. The external surfaces were faired arbitrarily (but similarly port and starboard) to blend into the endwall external surfaces of the nacelle proper.

Most of the tests reported here were made with intake 1 and cowl B. It will be noted in the text when this was not the case.

3.2 Test conditions

Tests were made at zero incidence of the horizontal fuselage datum in the 3ft × 3ft wind tunnel over a Mach number range 0.6 to 2.0. Free stream total pressure was varied to give the following values of Reynolds number, based on the inlet height, h_e:-

M_∞	Subsonic	1.41	1.71	2.00
$R_e/10^6$	0.78	0.46	0.39	0.29

Transition of the boundary layers on the cowl and endwall external surfaces was not fixed by artificial means. If the external flow is attached (as might be expected under conditions of high internal flow), because of the low Reynolds numbers of the tests, transition will not necessarily occur at the intake lips. However because of the small model scale and consequent fineness of the lips, fixing transition in this vicinity by a roughness band would introduce a substantial modification both to the lip thickness and initial cowl external

---

* The upper and lower walls of the intake in the present orientation with respect to the fuselage are termed 'endwalls'.

profile and thus possibly alter the drag characteristics of the model. If however, because of spillage of air from the intake, separation of the flow from the cowl external surface does occur, it might be expected that, on reattachment, the boundary layer would be turbulent and transition would be fixed in this way. Simple calculations indicate that the difference in total external drag, between a case in which there is a fairly extensive region of laminar flow on the cowl external surface and one in which transition occurs at the cowl lip, is of the order of $\Delta C_{D_E} = 0.02$. Transition was fixed close to the compression surface leading edges by bands of distributed roughness, particularly for tests at supersonic speeds to ensure that laminar boundary layers and shock interactions did not occur.

A throat bleed slot was included in the design of the model, Fig.8a and b, and the nacelle design allows for the control and measurement of one bleed flow. However the primary function of throat bleed flow in an intake is to improve its internal performance and unless its presence affects the external flow, it will have no influence on external drag. Because of additional errors in external drag which would be introduced from an assessment of internal drag of the bleed, present tests were made with zero bleed flow.

3.3 Flow environment

A preliminary experiment was made using the fuselage without intakes (Fig.2b) to measure the flow field at a position just upstream of the inlet plane. This plane was surveyed over the area of the intake in sufficient detail to provide information on fuselage boundary layer thickness and local Mach number distribution external to the boundary layer. Results of this survey are shown in Fig.9. The thickest fuselage boundary layer was measured at $M_\infty = 2.0$ and to keep the intake clear of the boundary layer at all Mach numbers, this thickness defined the depth of the diverter passage, h_D, at a value $h_D/h_e = 0.19$. Contour lines of constant local Mach number are shown for each supersonic test condition in the figure, giving the following mean values of local Mach number, M_L:-

M_∞	1.41	1.71	2.00
M_L	1.46	1.75	2.01 .

4 DISCUSSION OF RESULTS

4.1 Intake performance

Results are shown in Fig.10a to g for the intake configuration 1 with $r_\ell/r_e = 0.011$ and $\delta_2 = 0^\circ$ and with both swept and unswept endwalls. Mean pressure recovery and total external drag coefficient are plotted as functions of intake mass flow ratio and actual experimental points are included to indicate typical scatter of the data about mean curves. Calculated values of maximum mass flow ratio are included at each Mach number and at supersonic speeds calculated values of shock pressure recovery are indicated.

At subsonic speeds the maximum internal flow which can be achieved, assuming that the duct exit is adequately sized, is limited by choking of the flow in the intake throat and it is for this condition that the maximum values shown in the figure are calculated (assuming that the geometrical minimum area is the actual flow area). The precise establishment of maximum mass flow ratio by measurement is difficult. The actual experimental results give maximum values which appear high relative to those calculated and at the higher Mach numbers, exceed them for some model configurations. If the duct throttle is opened beyond the point at which the intake throat has choked, there should be no further increase in mass flow. However, when this is done, measurements of total pressure at the measuring station show a marked deterioration in distribution of the flow, the distributions becoming very much worse than those experienced during calibration. It is thought therefore that the calibration factor K_f (see section 2.3) is no longer valid and its application allows a larger mass flow ratio to be measured than is actually present. This seriously affects the corresponding external drag values. To resolve it, the assumption is made that, because of viscous effects, there is a throat discharge coefficient of 0.98 and thus the maximum mass flow ratio which can be accepted in the experiment is $0.98\left(A_\infty/A_e\right)_{\text{calculated}}$. In the results presented, drag coefficients obtained at measured mass flow ratio equal to or less than this value are assumed correct. For values obtained at higher measured mass flows, if they are corrected by an increment in C_{D_E} where:-

$$\Delta C_{D_E} = 2\left[\left(A_\infty/A_e\right)_{\text{measured}} - 0.98\left(A_\infty/A_e\right)_{\text{calculated}}\right] \qquad (10)$$

then the resulting values (now effectively corrected to the assumed maximum possible flow of $0.98\left(\left(A_\infty/A_e\right)_{\text{calculated}}\right)$, are found to align very closely with the values actually measured at this mass flow and thus, the limiting point in the data presented is established in this way. This is illustrated with some typical experimental data in Fig.11. It is concluded therefore that the drag values quoted at $0.98\left(A_\infty/A_e\right)_{\text{calculated}}$ are correct but that this mass flow ratio may not be precisely the choking value.

At supersonic speeds maximum values of mass flow ratio are controlled by the geometry of the external shocks. Theoretical values of maximum mass flow ratio included in Fig.10e to g, are calculated assuming the theoretical shock geometry, with attached compression surface and cowl lip shocks, for the intake in a uniform airstream of Mach number equal to M_L. These values are then referred to free stream conditions M_∞, so that they may be compared with measured values. Theoretical values of maximum mass flow ratio are greater than those measured and it has been proposed[5,6] that better agreement is achieved if values are calculated for a deflection equivalent to the wedge angle plus 1°. If this proposition is applied to the present results, agreement is found to be good at $M_\infty = 2.00$ but at $M_\infty = 1.41$ and 1.71 the addition of 0.5° would give better agreement.

In most cases the external drag is found to remain constant when the intake is operated in a supercritical condition but occasionally there is evidence of an uncertain drag level e.g. the configuration with swept endwalls at $M_\infty = 1.71$, (Fig.10f). This may be associated with small variations in measured values of maximum mass flow ratio which arise because of poor flow distributions.

4.2 Cowl external surface flow under spilling conditions

To investigate the flow over the external surface of the cowl associated with spillage of air from the intake at subsonic speeds, tests were made using the oil flow technique. Photographs of flow patterns obtained are shown in Fig.12 which correspond with conditions of intake flow indicated on the external drag curves of Fig.10a. At high mass flow ratio (low spillage), the flow is characterised by a small bubble separation at the cowl lip with attached streamwise flow over the remainder of the cowl surface (patterns 1 and 2). As spillage increases the extent of the separation increases until most of the cowl surface is in a region of separated flow (patterns 4 to 6). These patterns illustrate the three-dimensional flow which occurs within this type of separation and may be compared with the surface flow pattern beneath an oblique shock wave incident on a flat plate boundary layer[7]. A schematic interpretation of the cowl flow, annotated in a manner similar to that used in Ref.7, is shown in Fig.13 for the intake configuration with swept endwalls. In this case the flow over the endwalls separates at the sharp swept leading edge to form a vortex system which appears to be independent of the cowl separation. Reattached flows from both cowl and endwall separations meet along the line characterised in patterns 5 and 6 by the thick streak of oil which originates from each corner of the cowl. When the endwalls are unswept, the flow on these surfaces appears to be part of a single separated flow region involving the cowl flow, giving continuous surface streamlines around the external corners of the cowl (patterns 3 and 4).

4.3 Effect of swept endwalls

Physical differences necessary on the model between swept and unswept endwall configurations are illustrated in Fig.14. Swept endwalls introduce additional wetted area and with the present model, alter appreciably the external profile of the unswept configuration. Material to be added is indicated on the figure and the side elevation of a section close to the fuselage, (Fig.14b), shows the relative steepness of the external profile in this region for the unswept configuration.

Results presented in Fig.10 indicate differences in performance between the two configurations and considering firstly results at subsonic free stream Mach number, Fig.10a to d, the swept endwall configuration is seen to give a lower drag at full flow but a steeper rise in drag (spillage drag) as flow is reduced than the other. It is difficult to establish the reason for the lower drag at full flow of the swept configuration; a small increase in drag might have been expected from the additional external wetted area but it would appear that either the modified external profile or perhaps less likely, the fact that lateral flow is largely prevented by the swept endwalls is the dominating factor and results in a net reduction of drag. For the intake with unswept endwalls, spillage is free to take place both over these surfaces and over the cowl whereas sweeping the endwalls has the effect of preventing lateral flow and thus, to a large extent, confining the spilled flow to the cowl. At points 4 and 5 in Fig.10a, the two configurations produce similar values of external drag for differences in internal flow of $\Delta A_\infty/A_e \triangleq 0.13$. Corresponding cowl surface flow patterns, Fig.12, indicate a similar extent* of flow separation in the two cases and similar values of flow spilled over the cowl and cowl drag might therefore be expected. If this is so, the difference noted in internal flow is a consequence of lateral spillage over the unswept endwalls for no penalty in drag. Little penalty might be expected because firstly, the endwalls are operating at relatively low spillage $\left(0.13 \frac{A_\infty}{A_e} \text{ between them}\right)$ and secondly, their external profile has a high initial slope.

At supersonic speeds the effects of endwall geometry on intake performance are shown in Fig.10e to g. Considering maximum (supercritical) values of mass flow ratio, differences measured are usually associated with spillage over the endwalls. McGregor[6] has proposed a parameter which, when the oblique shock is outside of the cowl lip, is shown to correlate the difference between theoretical and measured values of maximum mass flow ratio. This parameter is a function of intake geometry, external shock geometry and the difference in static pressure between air inside the compression field and that outside it. Using data from Ref.6 increments in mass flow ratio have been obtained at each test Mach number for the two present configurations of endwall and the difference between these gives spillage resulting from the geometry change. Increments obtained in this way are compared with those measured in the following table:-

M_∞		1.41	1.71	2.00
$\Delta A_\infty/A_e$	predicted (Ref.6)	0.052	0.040	0.037
$\Delta A_\infty/A_e$	measured	0.022*	0.031	0.028

Increments in maximum mass flow ratio for change in endwall configuration from unswept to swept.

* Shock geometry is a little uncertain at this condition as detachment of the first oblique shock occurs theoretically at a Mach number of 1.43, which is between $M_\infty = 1.41$ and $M_L = 1.46$.

In each case the increment predicted is greater than that measured, implying that the measured difference can be wholly accounted for by additional spillage over the endwalls of the unswept configuration.

---

* Assessed by the positions on the cowl surface of reattachment lines.

External drag curves at $M_\infty = 1.41$, Fig.10e, show similar trends to results obtained at subsonic speeds in that a considerably lower drag is measured at full flow for the configuration with swept endwalls but the rate of rise of spillage drag is greater than for the other configuration. Differences in drag at full flow may be ascribed to changes in wave drag which result from changes in external profile of the endwalls, illustrated in Fig.14b. Differences in slope of the curves indicate that a greater reduction in cowl drag with spillage occurs for the configuration with unswept endwalls. At $M_\infty = 1.71$ and 2.00 there is little difference between the slopes of the drag curves indicating that no benefit in cowl drag is obtained from the steep external profile of the unswept configuration at these Mach numbers. There is however an increment in drag at full flow which again is associated with the differences in wave drag of the two external profiles. At $M_\infty = 2.0$ the difference in measured drag between the two configurations at full flow is $\Delta C_{D_E} = 0.075$. This increment contains the pre-entry drag associated with the difference in maximum measured flow, which may be calculated and for 3% spillage, is about 0.007. Thus a net wave drag increment of $\Delta C_{D_W} = 0.068$ is measured. Using data for calculating the wave drag of parabolic forebodies contained in Ref.8, the difference in wave drag has been calculated for the two profiles shown in Fig.14b. It has been assumed that the endwalls constitute one quarter of the corresponding body of revolution and this gives a wave drag increment for the endwalls of $\Delta C_{D_W} = 0.087$. Thus a ratio of changes of wave drag due to change in endwall geometry is:-

$$\frac{\text{estimated change}}{\text{measured change}} = 1.28 \quad .$$

This might be expected because the estimated change will obviously be too great as the difference between the profiles for the model configurations varies from that shown in Fig.14b at the inboard section, to nothing at the corners of the intake (indicated on Fig.14a by arrow A).

4.4 Effect of compression surface geometry

Results at subsonic speeds are presented in the form of external drag curves for various values of second wedge angle δ_2; in Fig.15 they are for the intake with unswept endwalls and in Fig.16 with swept endwalls.

These data confirm the general result indicated in Ref.1*, that the external drag at full flow remains substantially constant when compression surface geometry is varied. Thus, some flow spillage may be achieved with little drag penalty, provided that the compression surface is adjusted to keep the throat Mach number high. Results for the configuration with unswept endwalls at $M_\infty = 0.9$, Fig.15b, show a rather larger variation in full flow drag with δ_2 than other cases but nevertheless, the advantage of ramp elevation is still illustrated. Spillage drag (or the slope of the external drag curves) increases with increasing δ_2 causing the external drag curves to converge at low mass flow ratio, i.e. in the region $A_\infty/A_e = 0.25$. Effects of compression surface geometry on full flow drag and relative spillage drag appear to be largely independent of endwall configuration in that similar trends occur with both.

At supersonic speeds, variation in compression surface angle is considered firstly in terms of its effect on the full flow performance of the intake. In Fig.17 maximum mass flow ratio and drag increment relative to the full flow drag value of the configuration with swept endwalls and $\delta_2 = 0^\circ$, are plotted as functions of δ_2 for each test Mach number.

The oblique shock wave at a 10° wedge will detach at a free stream Mach number just less than 1.43. Thus the present intake at $M_\infty = 1.41$ ($M_L = 1.46$) is close to this condition. Assuming this first oblique shock is attached, both the second oblique shock and the cowl shock are detached when δ_2 is greater than 1° and thus, for experimental data at $\delta_2 = 4.75^\circ$ and 11.5°, these shocks will be detached whereas for $\delta_2 = 0^\circ$ they might not be. The maximum theoretical mass flow ratio (for $\delta_2 = 0^\circ$) indicated on Fig.17a is calculated for attached shocks at $M_L = 1.46$.

Assuming that for values of $\delta_2 > 1^\circ$ there is a single detached normal shock ahead of the intake, increments in drag have been calculated from:-

$$\Delta C_D = \Delta\left(\frac{A_\infty}{A_e}\right)_{max} \left(\frac{\Delta p}{q_\infty}\right) \tag{11}$$

where $\Delta\left(\frac{A_\infty}{A_e}\right)_{max}$ is the deficit in mass flow ratio from the value for the intake with swept endwalls and $\delta_2 = 0^\circ$, and Δp is the static pressure rise across a

---

* The data quoted in Ref.1 were for the present model but with a sharp cowl lip; $r_\ell/h_e = 0.002$.

normal shock at $M_L = 1.46$. These values are plotted as a function of δ_2 in Fig.17a and compare well with the experimental data for this configuration. The increment in drag apparent from the change in configuration to unswept endwalls arises from both the wave drag associated with the changed external profile (see previous section) and, at low values of δ_2, the additional spillage drag associated with the decreased mass flow ratio.

At $M_\infty = 1.71$ ($M_L = 1.75$) the second oblique shock theoretically crosses the cowl lip at a δ_2 value of just less than 1° so that as δ_2 is increased beyond this the mass flow ratio decreases because of supersonic spillage behind this shock. The cowl lip shock theoretically becomes detached at a value of $\delta_2 \triangleq 6.2^\circ$ while the second oblique shock detaches at a theoretical value of $\delta_2 \triangleq 9.7^\circ$. The curves showing measured maximum mass flow ratio (Fig.17b) indicate similar trends with δ_2 to the calculated curve but with a decrement for the configuration with swept endwalls, as discussed in section 4.3. A further decrement associated with the configuration change from swept to unswept endwalls (also discussed for $\delta_2 = 0^\circ$ in section 4.3) is observed but only when theoretically all shocks are attached. When shocks are detached, e.g. for $\delta_2 = 11.5^\circ$, mass flow ratios measured for the two configurations are identical. Probably this is because the effect of removing the swept endwalls is to reaccelerate the flow behind the oblique shock by allowing lateral expansion and thus, possibly allowing reattachment of the cowl lip shock. In this case, increased spillage due to removal of the swept endwalls is balanced by the elimination of spillage behind the detached shock at the cowl lip.

At this Mach number increments in drag are calculated for shock geometries at values of δ_2 for which all shocks are theoretically attached. The measured drag for the configuration with swept endwalls is a little greater than that calculated which, it might be argued, is reasonable because the maximum measured flow is less than the theoretical value. However when the swept endwalls are removed the increase in drag is much greater than a *pro rata* decrease of maximum flow would suggest. If it is assumed that, with $\delta_2 = 11.5^\circ$, increments in pre-entry drag are similar because maximum flows are similar, then the additional drag for the configuration with unswept endwalls must be due to an increased cowl wave drag. This gives an increment in cowl drag of $\Delta C_{D_{\text{cowl }0}} \triangleq 0.08$.

At $M_\infty = 2.00$ the cowl lip shock theoretically becomes detached at a value of $\delta_2 \triangleq 10.4^\circ$ while the second oblique shock remains attached to a value of

δ_2 beyond the experimental maximum. This oblique shock theoretically crosses the cowl lip at $\delta_2 \triangleq 8^\circ$ and therefore results for configurations with $\delta_2 = 0^\circ$ and 4.75° would be expected to show identical values of maximum mass flow ratio and drag. Slightly lower values of maximum flow and slightly higher values of drag are in fact measured with $\delta_2 = 4.75^\circ$ but the magnitudes of differences (particularly for the configuration with swept endwalls) are similar to the accuracy of the experiment. When the cowl lip shock is theoretically detached ($\delta_2 > 10.4^\circ$) values of maximum flow for the two configurations of endwall are similar, giving an increment in cowl drag, at this Mach number, of $\Delta C_{D_{\text{cowl }0}} = 0.05$ to 0.06.

Variation of drag with spillage at supersonic speeds is shown for intakes with unswept endwalls in Fig.18 and with swept endwalls in Fig.19. For each combination of intake geometry and local Mach number at which all shocks are theoretically attached at maximum flow, values of pre-entry drag, $C_{D_{\text{pre }0}}$, are included in Fig.19 which, referring in Fig.20a are calculated from:-

$$C_{D_{\text{pre }0}} = \left[\frac{p_2 - p_\infty}{q_\infty}\right]\frac{A_2}{A_e} + \left[\frac{p_3 - p_\infty}{q_\infty}\right]\frac{A_3}{A_e} \quad . \tag{12}$$

Also included at Mach numbers of $M_\infty = 1.71$ and 2.00, are curves (drawn for $\delta_2 = 0^\circ$) which predict spillage drag by calculation. For these the variation of the position of the intake normal shock with mass flow ratio is estimated[10] and at a mass flow ratio equal to or less than the value which gives a shock geometry as sketched in Fig.20b it is assumed that all spillage is subsonic (i.e. downstream of the normal shock). The total spillage drag is then given by:-

$$C_{D_{\text{spill}}} = \left[\frac{p_4 - p_\infty}{q_\infty}\right]\left[1 - \frac{A_\infty}{A_e}\right] \quad . \tag{13}$$

At both $M_\infty = 1.71$ and 2.00 the measured rate of drag increase with spillage is less than that predicted by this method of calculation.

4.5 Effect of cowl lip radius

Early in the supersonic test programme cowl A split at the junctions of the cowl and endwalls under aerodynamic loading and hence no supersonic data were obtained with this configuration. For this intake therefore, investigation into the effects of cowl lip radius were confined to tests at subsonic speeds. Results obtained are shown in Fig.21 for both intakes 1 and 2, each with cowls A and B and with unswept endwalls. Included are results presented in Fig.10 of Ref.1 which were for intake 2 at $M_\infty = 0.70$. Additional results presented here serve to confirm the conclusion of that reference that, at high internal flow, values of drag for the sharp lip cowl* are higher than those for a cowl whose lip is slightly blunted. As spillage increases the difference becomes smaller and at spillages greater than $\Delta A_\infty/A_e = 0.15$ to 0.20 below full flow, spillage drag is no longer sensitive to lip radius. As discussed in section 4.2 the external surface flow at subsonic speeds is characterised by a small bubble separation at the lip at high values of internal flow. Cowl drag under these conditions is presumably a function of the presence and extent of this separation which in turn will be influenced by the lip radius. At lower mass flow ratios where the separation is extensive, lip radius is no longer of significance.

4.6 Intake drag as a function of inlet** flow conditions

Observations have shown that the drag of an intake under spilling conditions is associated with separations of flow from the external surface of the cowl which, to some extent, is dependent on cowl lip geometry. These separations must also have some dependence on the local flow direction at the cowl lip and this is presumably controlled by both spillage quantity and total turning of the flow due to the presence of a compression surface. In Fig.21 drag data are shown for intakes 1 and 2 in both cases with a single 10° wedge compression surface but, by virtue of their different design shock-on-lip Mach numbers, have different values of inlet area A_i. In Fig.22 external drag at $M_\infty = 0.70$ for these configurations is plotted as a function of inlet mass flow ratio A_∞/A_i where:-

$$\frac{A_\infty}{A_i} = \left(\frac{A_\infty}{A_e}\right) \Bigg/ \left(\frac{A_i}{A_e}\right) \qquad (14)$$

---

* In this context the word 'cowl' really includes the unswept endwalls.

** The 'inlet' station is defined by 'i' in Fig.8a.

and

$$\frac{A_i}{A_e} \text{ for intake 1} = 0.721$$

$$\frac{A_i}{A_e} \text{ for intake 2} = 0.781 \quad .$$

These data for the two configurations collapse on to a single curve indicating that for a given flow turning (total compression surface angle, $\delta_1 + \delta_2$) external drag is related uniquely to inlet mass flow ratio. If drag results obtained for intake 1 with various values of δ_2 are plotted as a function of inlet mass flow ratio, any differences between the curves will be an indication of additional effects due to flow turning by the compression surface. This is done for $M_\infty = 0.60$ in Fig.23 using the data previously shown in Fig.15a. To make it easier to identify any differences, spillage drag rather than total external drag is plotted because this eliminates the small variations of drag measured at full flow with the various configurations of δ_2. The data for $\delta_2 > 0^\circ$ collapse on to a single curve at high inlet flow but at lower values there is a divergence with the higher values of δ_2 giving higher drag. Results for the configuration with $\delta_2 = -10^\circ$ do not conform to this pattern for reasons which, at present, are not clear.

4.7 Pressure drag of installed intake

Methods are available by which wave drag of ducted forebodies of revolution in supersonic flow may be predicted and also by which drag of two-dimensional surfaces of parabolic shape may be calculated. These methods apply to idealised configurations and when, in practice, the intake is neither a body of revolution nor two-dimensional it is often not sensible to use them to predict wave drag. However, by using a combination of calculated and measured drag increments, it is possible to obtain an estimate of the pressure drag of the installed cowl, C_{D_c} (inst), and this has been done for the present intake with cowl B and $\delta_2 = 0$, at full flow for each test Mach number. Results of this analysis are given in Table 5 and using the notation of drag coefficients indicated in the table:-

$$C_{D_c}(\text{inst}) = C_{D_E} - \left[C_{D_{(F+C)}} + C_{D_f}(\text{inst}) + C_{D_w}(\text{div}) + C_{D_{\text{pre }0}}\right] \tag{15}$$

where C_{D_E} = measured external drag of fuselage + canopy + diverters + intakes at full flow

$C_{D_{(F+C)}}$ = measured drag of fuselage + canopy only

$C_{D_f}(\text{inst})$ = skin friction drag of installed nacelles which, referring to Fig.24, is the sum of the skin friction drag coefficients* of:-

(area E + area F_I + area D - area B)

$C_{D_w}(\text{div})$ = wave drag of diverter at supersonic speeds derived from data quoted in Ref.1. (Diverter pressure drag was found to be zero at subsonic speeds[1].)

$C_{D_{\text{pre }0}}$ = calculated pre-entry drag at maximum flow assuming that all shocks are attached.

Drag increments contained in Table 5 are plotted as functions of Mach number in the upper graph of Fig.25 to illustrate the analysis more readily. These data show a constant level of drag at $M_\infty = 0.6$, 0.7 and 0.8 with virtually zero pressure (or form) drag for the installed intakes. At $M_\infty = 0.9$ signs of the expected transonic drag rise have appeared with evidence of an increasing installed cowl pressure drag.

In the lower graph of Fig.25 the installed cowl pressure drag derived in this analysis is compared at supersonic speeds with theoretical values calculated for an isolated ducted body of revolution. The derived data show increases in drag coefficient with increasing Mach number whereas, from theoretical considerations, a decreasing trend would have been expected. Derived values contain any drag changes associated with interference effects which result from the installation and these, together with the inadequacy of the theoretical estimates in this application, must account for the conflicting trends observed.

5 COMPARISON OF CALCULATED AND MEASURED DRAG AT SUBSONIC SPEEDS

The major difficulty in any comparison of calculated and measured values of drag at subsonic speeds is the establishment of a drag datum for the calculated data. One such datum is defined for the present model with $\delta_2 = 0^\circ$, by a method illustrated at Mach numbers of 0.6 and 0.9 in Fig.26. Skin-friction

---

* Skin friction drag coefficients have been calculated using flat plate data[3] and therefore, because of the three-dimensional nature of the model, some reservation must be placed on their accuracy.

drag of the complete model may be calculated and from potential flow considerations, should remain invarient with change of internal flow. Skin-friction drag is shown in Fig.26 as the sum of calculated values for the fuselage plus canopy, C_{D_f} (F+C), and the installation skin-friction drag, C_{D_f} (inst), defined in section 4, and is represented by horizontal lines which terminate at the choking mass flow ratio of the intakes. Making simple assumptions for the mean pressure on the wedge compression surface, a pre-entry drag may be calculated by analysis of the forces for a control volume bounded by the internal flow between a station at infinity upstream and the inlet station, i, see Fig.8a. Pre-entry drag is given by:-

$$C_{D_{pre}} = (p_m - p_\infty) \frac{1}{q_\infty} \frac{A_R}{A_e} + \left[q_i + \tfrac{1}{2} (p_i - p_\infty)\right] \frac{2}{q_\infty} \frac{A_i}{A_e} \cos\theta - \frac{2A_\infty}{A_e} \qquad (16)$$

where it is assumed that $p_m = \left(\frac{p_i + p_\infty}{2}\right)$.

Neglecting viscous effects and assuming $\cos\theta = 1$, when $A_i = A_\infty$, $p_i = p_\infty$ and $C_{D_{pre}}$ will be equal to zero. This will occur at a mass flow ratio given by:-

$$\frac{A_\infty}{A_e} = \frac{A_i}{A_e}$$

which is a function of intake geometry and independent of Mach number. At this condition it is argued that the total drag of the model is given by the skin-friction drag, and pre-entry drag curves are drawn in Fig.26 accordingly. Also included are curves showing the variation in thrust force which would have to be developed on the cowls in order to balance the pre-entry drag and provide a net drag which is invariant with mass flow ratio.

These calculated data therefore, provide a framework onto which measured total external drag values may be plotted, as in Fig.26, but it is felt that any more rigorous comparison cannot be made. It must be noted that, as well as including skin friction and spillage drags, measured data also contain form drags of both fuselage plus canopy and the intake installation. For the present model it is found that, at $M_\infty = 0.6$, these form drags are approximately zero[1] but at higher Mach numbers, ($M_\infty = 0.9$), where transonic effects are felt, they are significant.

6 CONCLUSIONS

An experiment is described from which measurements of drag associated with fuselage side intake installations are obtained at both subsonic and supersonic speeds. The model provides for versatility in the configuration of intakes which may be tested and it is concluded that standards of measurement are adequate for determination of increments in external drag resulting from flow spillage and from relatively small variations in intake geometry.

Tests on particular rectangular intakes, orientated so that their compression surfaces are vertical and adjacent to the fuselage, have shown that:

A at subsonic speeds:

(i) external cowl surface flow is characterised by a bubble separation at the lip at high internal flow, with attached streamwise flow over the remainder of the cowl surface. As spillage increases, the extent of the separation increases until most of the cowl external surface is in a region of separated flow;

(ii) a configuration with swept endwalls gives lower drag at full flow but a steeper rise in drag with spillage than one in which the endwalls are unswept;

(iii) when the inlet mass flow ratio (A_∞/A_i) is close to or greater than unity, external drag is virtually independent of second ramp angle δ_2. Thus a wide range of internal flows can be accommodated at substantially constant drag by adjusting δ_2, so that the inlet mass flow ratio is maintained close to this value or expressed in another way, so that the inlet Mach number remains substantially similar to that of the free stream;

(iv) when inlet mass flow ratio is close to unity, a sharp lip cowl ($r/h = 0.2\%$) gives higher drag than one with a blunter lip ($r/h = 1.1\%$). However, as mass flow ratio is reduced the difference disappears;

(v) for single wedge intakes whose compression surfaces have similar wedge angles but are positioned differently (i.e. the distance from the wedge leading edge to the plane of the cowl differs), spillage drag is shown to be a function of inlet mass flow ratio.

B at supersonic speeds:

(vi) drag, with the intake operating in a supercritical condition, is found to vary in a manner which would be predicted from consideration of changes in shock geometry associated with movement of the compression surface but measured absolute values are rather higher than would be expected from the theory;

(vii) calculation methods based on theoretical shock geometry are found to overestimate measured spillage drag which, at higher Mach numbers, is similar for intake configurations both with and without swept endwalls;

(viii) using both measured and calculated drag increments, pressure drag of the installed intakes has been derived. This is found not to vary with supersonic Mach number in a manner which would be predicted from theoretical considerations. Reasons for this are assumed to be associated with interference effects introduced by the installation and inadequacy of theoretical estimates for this application.

Table 1

ERRORS IN THE MEASUREMENT OF DRAG COEFFICIENTS INTRODUCED BY INSTRUMENT AND CALIBRATION ACCURACIES

M_∞	A_∞/A_e	Terms*				C_{D_I}	$C_{D_{bal}}$	$C_{D_{base}}$	C_{D_E}
		1	2	3	4				
0.6	0.762	** 0.0060	0.0011	0.0011	0.0044	0.0126	0.0020	0.0025	0.0171
	0.528	0.0060	0.0011	0.0011	0.0044	0.0126	0.0020	0.0025	0.0171
0.9	0.733	0.0060	0.0011	0.0011	0.0045	0.0127	0.0020	0.0025	0.0172
	0.537	0.0060	0.0011	0.0011	0.0045	0.0127	0.0020	0.0025	0.0172
2.0	0.860	0.0060	0.0017	0.0017	0.0067	0.0161	0.0030	0.0038	0.0229
	0.646	0.0060	0.0017	0.0017	0.0067	0.0161	0.0015	0.0038	0.0214

Term: 1 2 3 4

$$* \quad C_{D_I} = \frac{2A_\infty}{A_e} - \frac{p_f}{q_\infty}\frac{A_f}{A_e} + \frac{p_\infty}{q_\infty}\frac{A_f}{A_e} + \frac{1}{q_\infty}\frac{A_f}{A_e}\gamma p_f M_f^2$$

** 0.0060 represents an accuracy in coefficient of plus or minus 0.0060.

Table 2

DRAG COEFFICIENTS OBTAINED AT SUPERSONIC SPEED WITH INTAKE OPERATING IN A SUPERCRITICAL CONDITION

M_∞	A_∞/A_e	C_{D_E}	Scatter	M_∞	A_∞/A_e	C_{D_E}	Scatter	M_∞	A_∞/A_e	C_{D_E}	Scatter
1.41	0.717	0.916	±0.001	1.71	0.838	0.969	±0.004	2.00	0.912	0.850	±0.003
	0.717	0.918			0.839	0.966			0.912	0.844	
	0.717	0.916			0.838	0.966			0.913	0.845	
	0.717	0.916			0.839	0.967			0.913	0.845	
					0.839	0.968			0.913	0.849	
					0.838	0.965			0.912	0.847	
					0.838	0.965					
					0.838	0.961					

Table 3

SCATTER OF VALUES OF DRAG COEFFICIENT AT SUBSONIC SPEEDS

M_∞	A_∞/A_e	C_{D_E}	Scatter	M_∞	A_∞/A_e	C_{D_E}	Scatter
0.6	0.627	0.210	±0.0015	0.8	0.586	0.197	±0.0025
	0.623	0.210			0.583	0.197	
	0.619	0.213			0.580	0.202	
	0.612	0.210					
	0.604	0.213					
0.7	0.599	0.197	±0.002	0.9	0.583	0.220	±0.0015
	0.596	0.201			0.582	0.223	
	0.592	0.200			0.578	0.220	

Table 4

NON-DIMENSIONAL PROFILE OF COWL EXTERNAL SURFACE

x/X	0	0.038	0.076	0.152	0.227	0.303	0.379	0.454
y/Y	0	0.090	0.180	0.328	0.465	0.553	0.660	0.740
x/X	0.530	0.606	0.681	0.758	0.833	0.909	1.0	
y/Y	0.799	0.846	0.883	0.920	0.958	0.978	1.0	

Non-dimensional ordinates define external profile of cowl from an origin at point Z (see Fig.8c)

Table 5

ANALYSIS TO DERIVE INSTALLED COWL PRESSURE DRAG

M_∞	0.60	0.70	0.80	0.90	1.41	1.71	2.00
			Drag coefficients				
Fuselage + canopy drag $\left(C_{D_{(F+C)}}\right)$	0.151	0.151	0.160	0.191	0.442	0.416	0.454
Installation skin-friction drag $\left(C_{D_f}(\text{inst})\right)$	0.093	0.092	0.088	0.085	0.074	0.073	0.072
Diverter wave drag $\left(C_{D_W}(\text{div})\right)$					0.057	0.062	0.042
Pre-entry drag $\left(C_{D_{\text{pre } 0}}\right)$					0.109	0.059	0.035
Total of above	0.244	0.243	0.248	0.276	0.682	0.610	0.603
Measured drag $\left(C_{D_E}\right)$	0.237	0.251	0.258	0.298	0.785	0.820	0.830
Installed cowl pressure drag $\left(C_{D_C}(\text{inst})\right)$	-0.007	0.008	0.010	0.022	0.103	0.210	0.227

SYMBOLS

A	area
C_D	drag coefficient
D	drag
h	height
M	Mach number
P	total pressure
p	static pressure
q	dynamic pressure
r	radius
R_e	Reynolds number
V	velocity
γ	ratio of specific heats
δ_1	angle of first compression wedge (Fig.8)
δ_2	angle of second compression wedge (Fig.8)
Δ	increment
θ	angle
ρ	density

Suffixes

2	conditions downstream of first oblique shock
3	conditions downstream of intake normal shock
bal	balance
base	model base
c	cowl
e	'entry' (defined in Fig.8c)
E	external
f	duct measuring station
h	'highlight' (defined in Fig.8c)
i	'inlet' (defined in Fig.8a)
I	internal
ℓ	cowl lip
L	local flow conditions external to fuselage boundary layer
max	maximum
pre	pre-entry
pre 0	pre-entry at full internal flow
R	'ramp' (defined in Fig.8a)

SYMBOLS (concluded)

spill	spillage
w	wave
x	duct exit station
∞	free stream station

REFERENCES

No.	Author	Title, etc.
1	M.D. Dobson E.L. Goldsmith	The external drag at subsonic and supersonic speeds of fuselage side air intakes for strike fighter aircraft. ICAS Paper 70-49 also published as RAE Technical Memorandum Aero 1259 (ARC 32734) (1970)
2	I. McGregor	The characteristics and calibration of two types of airflow metering device for investigating the performance of model air intakes. RAE Technical Report 71212 (ARC 33894) (1971)
3	K.G. Smith	Methods and charts for estimating skin friction drag in wind tunnel tests with zero heat transfer. ARC CP No.824 (1964)
4	J.W. Britton M.D. Dobson	A note on the internal drag, lift and pitching moment of a ducted body. ARC CP No.1211 (1971)
5	J.D. Bryce B.J. Cocking	Some effects of Reynolds number on the performance of an air intake proposed for Concorde. NGTE Report R304 (ARC 31404) (1968)
6	I. McGregor	Some theoretical parameters relevant to the performance of rectangular air intakes with double-ramp compression surfaces at supersonic speeds. RAE Technical Report 71232 (ARC 33616) (1971)
7	J.E. Green	Interactions between shock waves and turbulent boundary layers. RAE Technical Report 69098 (1969)
8	L.E. Fraenkel	Curves for estimating the wave drag of some bodies of revolution based on exact and approximate theories. RAE Technical Note Aero 2184 (ARC 15685) (1952)
9	J.S. Mount	Additive drag on inlet cowls and its effect on aircraft performance. AGARDograph 103 (1965)

REFERENCES (concluded)

No.	Author	Title, etc.
10	W.E. Moeckel	Approximate method for predicting form and location of detached shock waves ahead of plane or axially symmetric bodies. NACA Technical Note 1921 (1949)

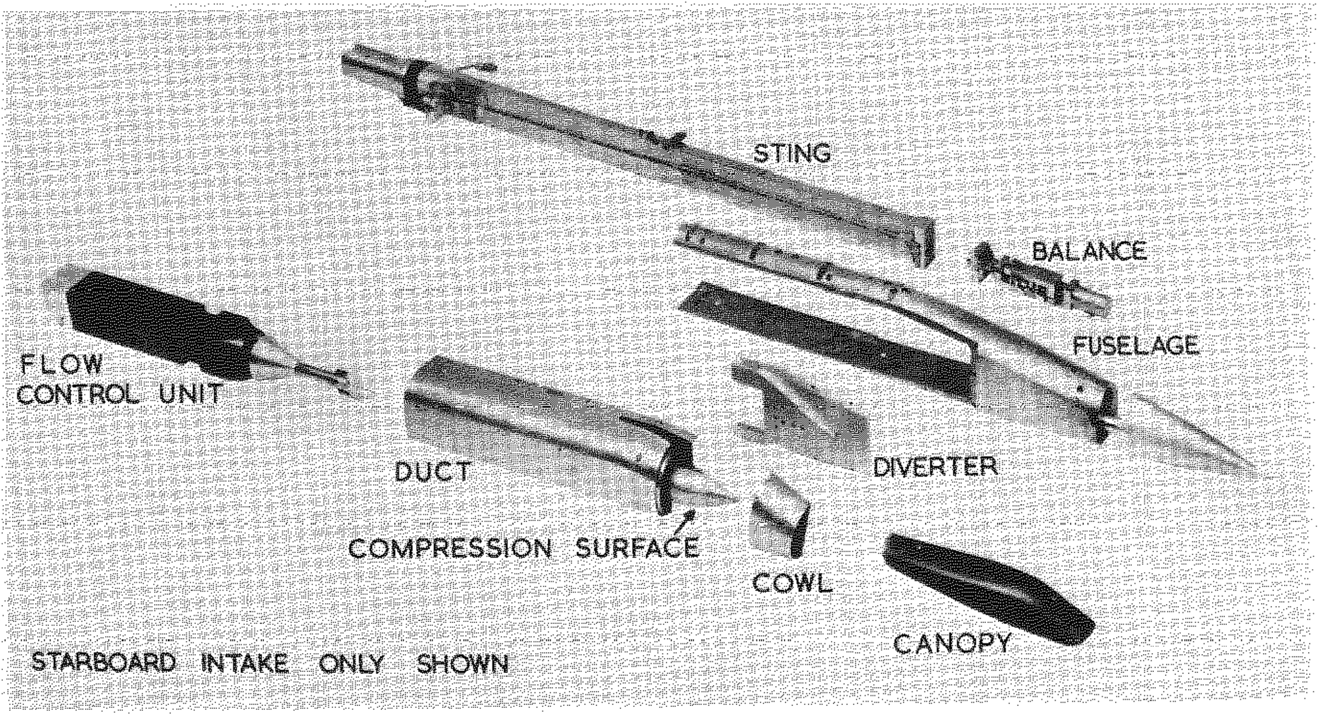

Fig.1 Exploded view of model

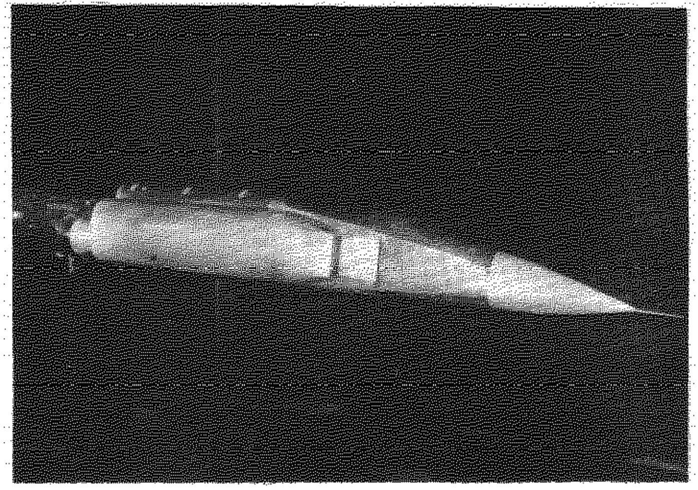

(a) With intakes

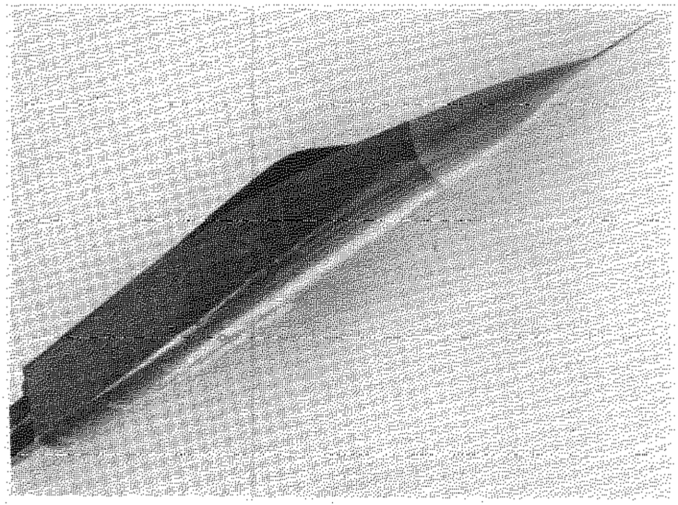

(b) With flat sides

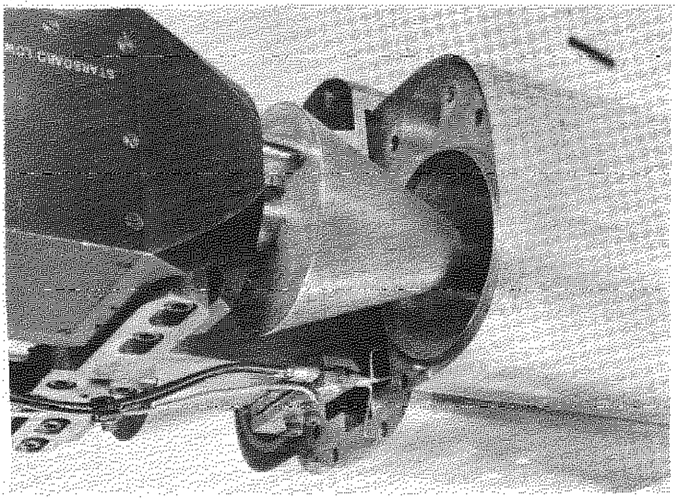

(c) Base region

Fig.2 The model

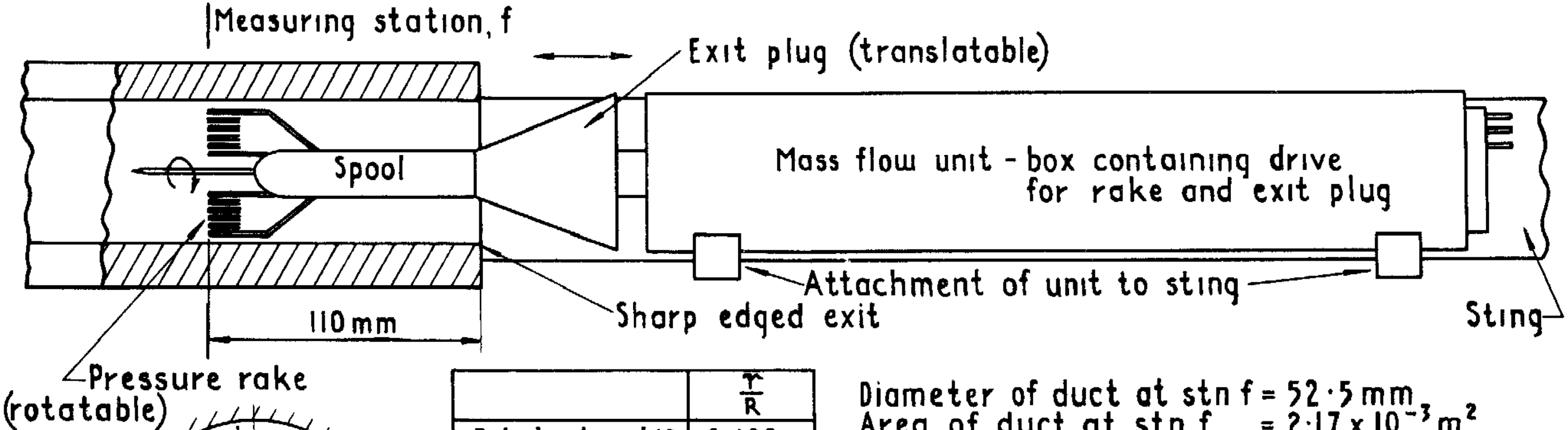

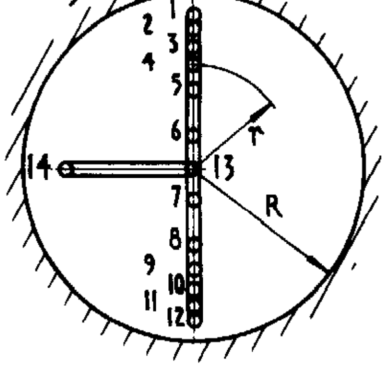

Section at f showing location of pressure tubes

	$\frac{r}{R}$
Pitots 1 and 12	0·188
Pitots 2 and 11	0·454
Pitots 3 and 10	0·591
Pitots 4 and 9	0·702
Pitots 5 and 8	0·796
Pitots 6 and 7	0·880
Static 13	0
Static 14	0·750

Diameter of duct at stn f = 52·5 mm
Area of duct at stn f = $2{\cdot}17 \times 10^{-3}\ \text{m}^2$
Diameter of spool = 18·5 mm

Fig 3 Arrangement for internal flow control and measurement

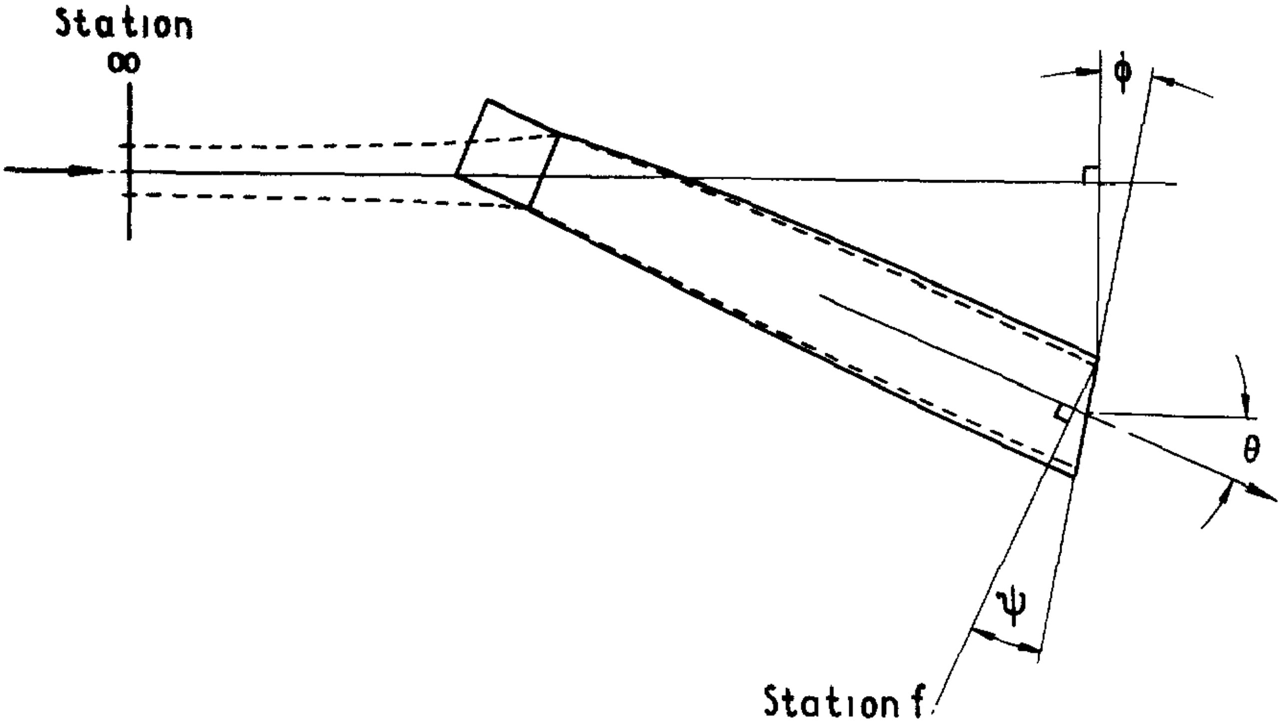

Fig. 4 Model for definition of standard internal drag (equation 2)

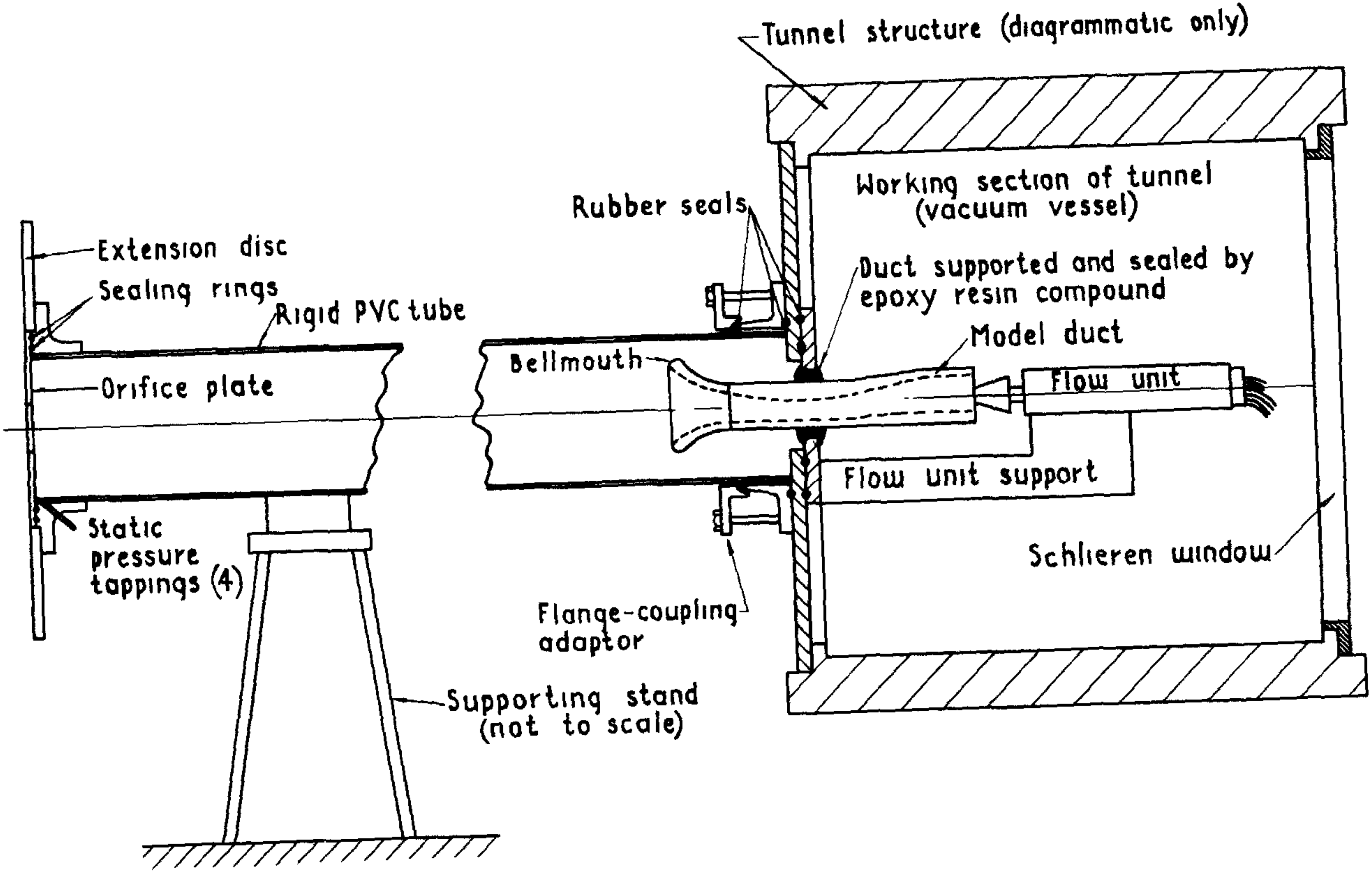

Fig.5 General arrangement of calibration rig

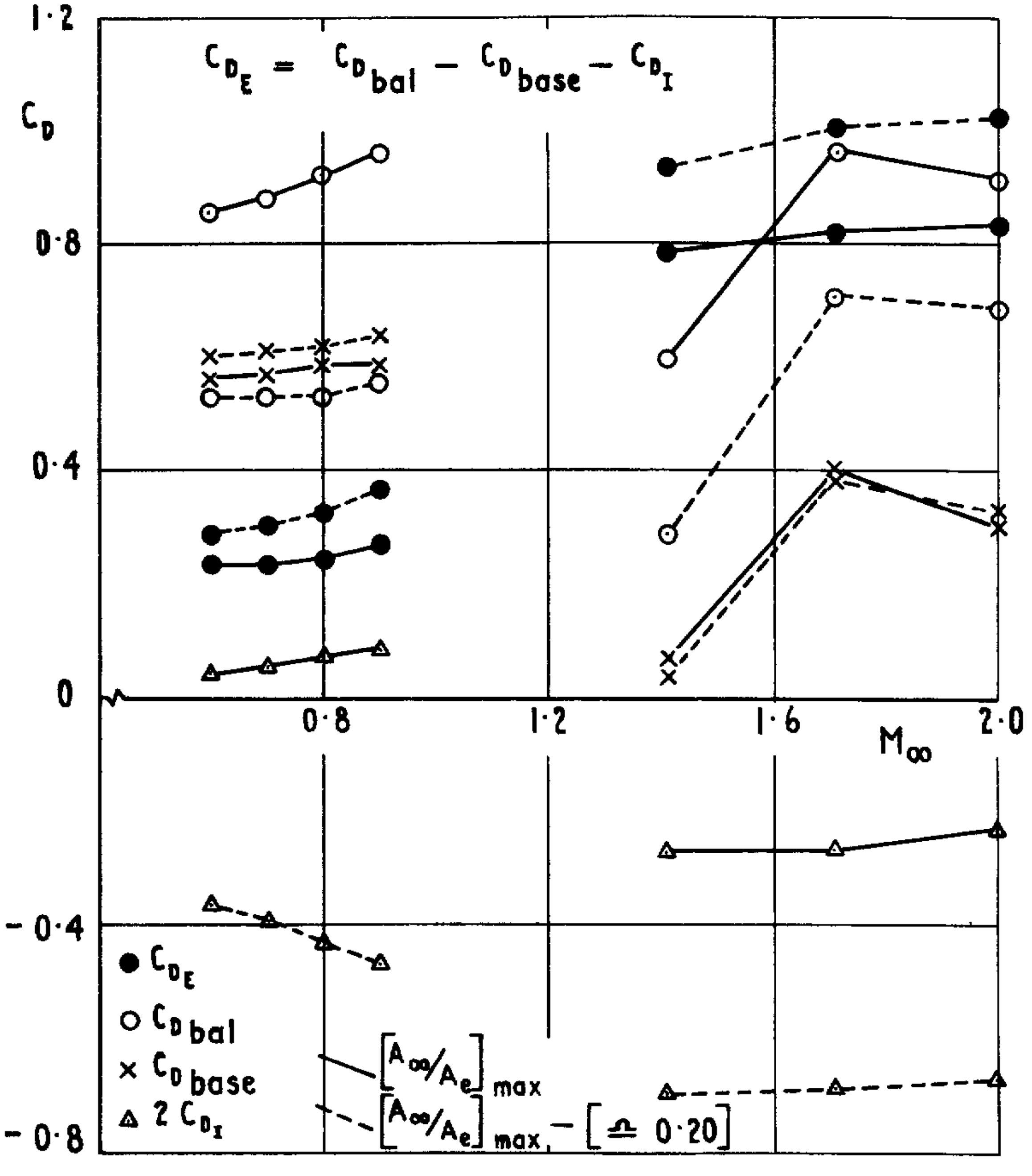

Fig. 6 Some relative magnitudes of measured drag components

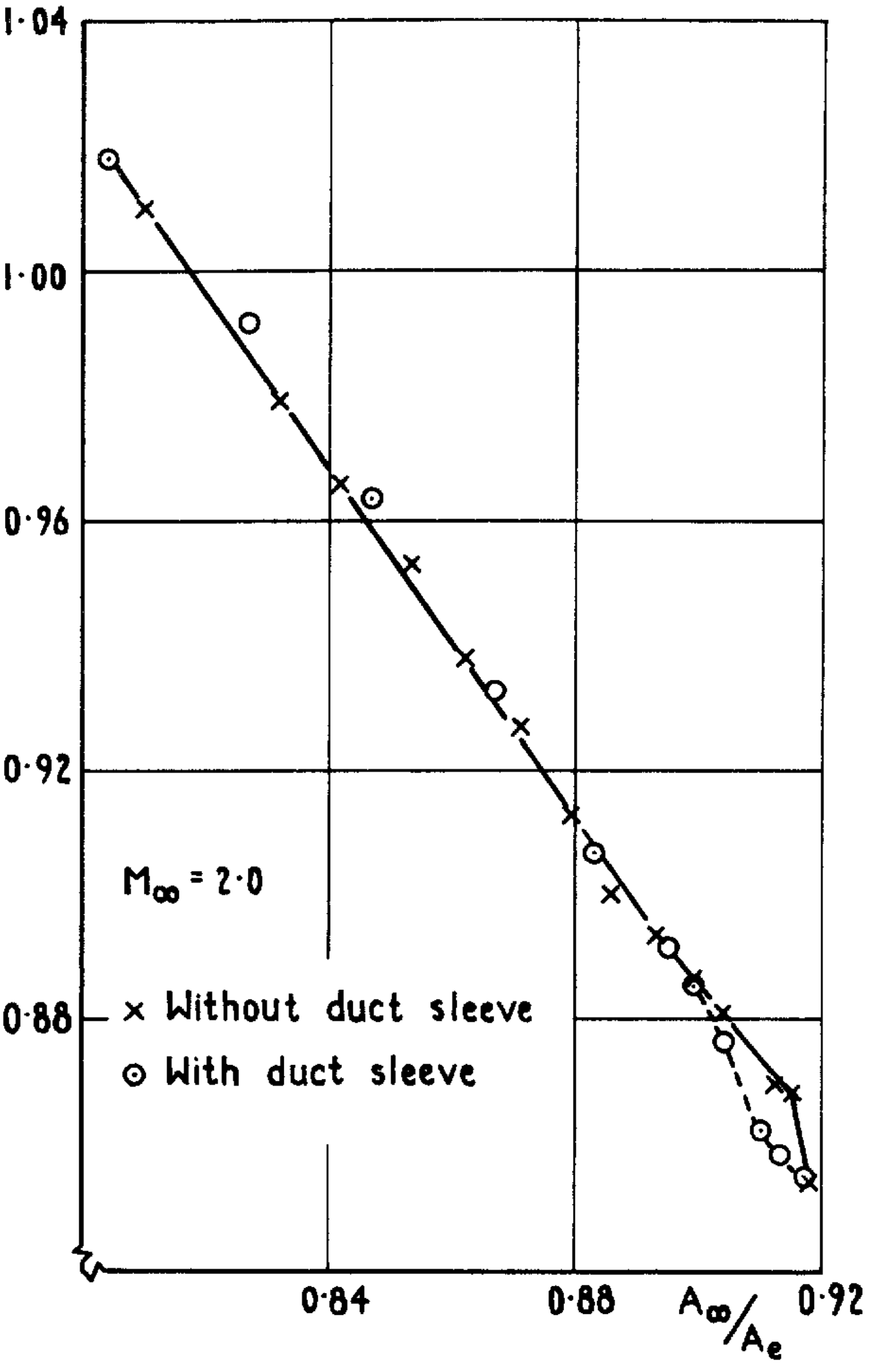

Fig.7 Comparison of external drag values measured with different internal flow conditions

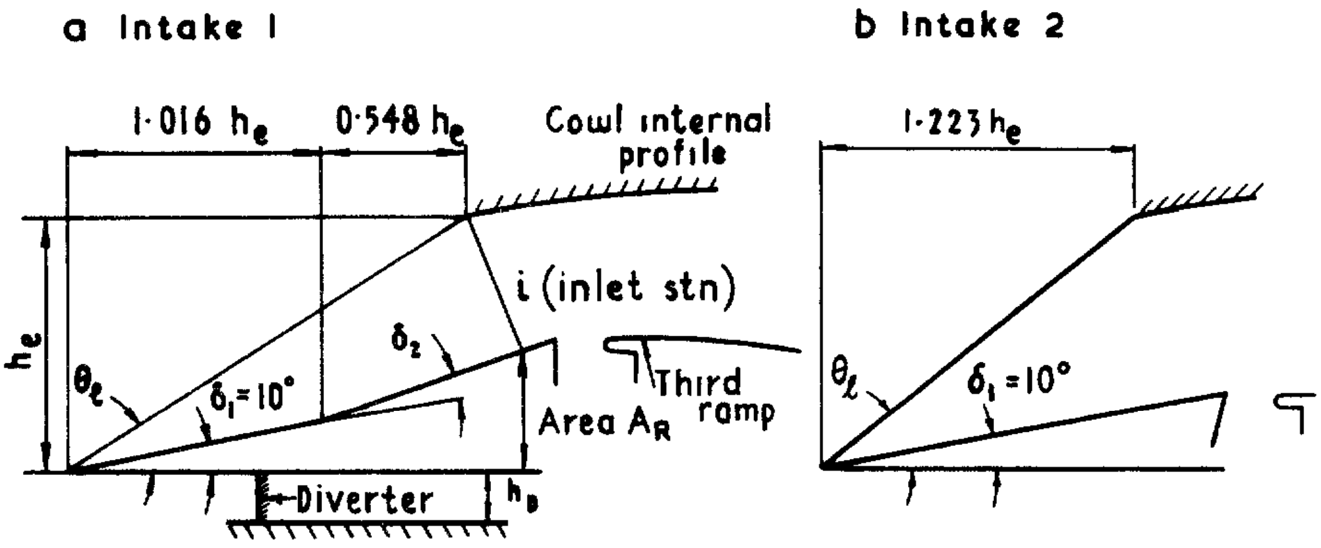

$\theta_\ell = 32{\cdot}6°$

$M_{\theta_\ell} = 2{\cdot}41$

δ_2 values $-10°$, $0°$, $4{\cdot}75°$, $11{\cdot}5°$

$\theta_\ell = 39{\cdot}27°$

$M_{\theta_\ell} = 2{\cdot}00$

Single 10° wedge

Intake size :- $h_e = 34{\cdot}26$ mm

Intake $\frac{\text{width}}{\text{height}} \left(\frac{W_e}{h_e}\right) = 1{\cdot}546$

c Cowl lip geometry

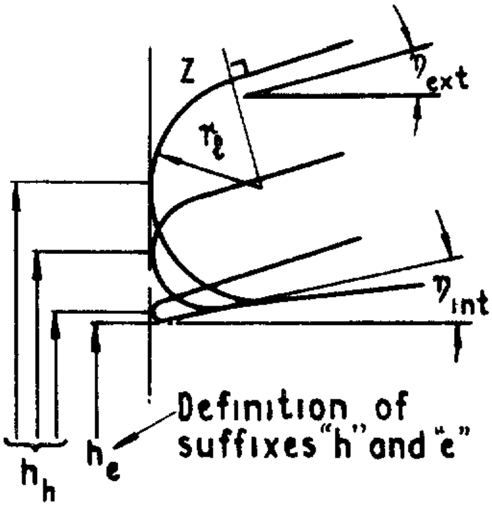

Cowl	A	B	C
r_ℓ / h_e	0·002	0·011	0·022
h_h / h_e	1·003	1·014	1·027
A_h / A_e	1·005	1·025	1·052

$\eta_{ext} = 18°$ $\eta_{int} = 13°$

Fig. 8 a–c Details of intake geometries

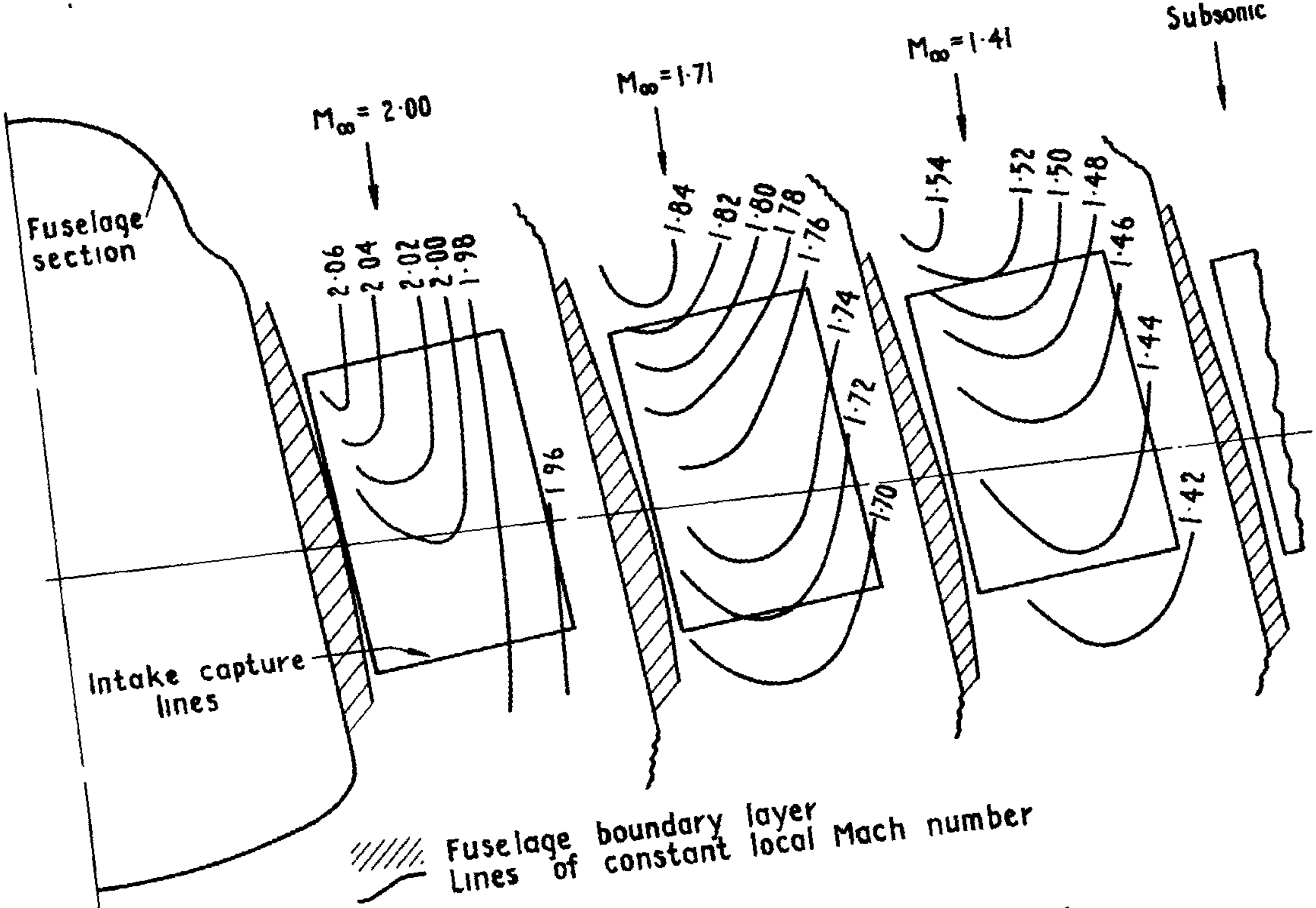

Fig.9 Flow fields at entry plane of intake

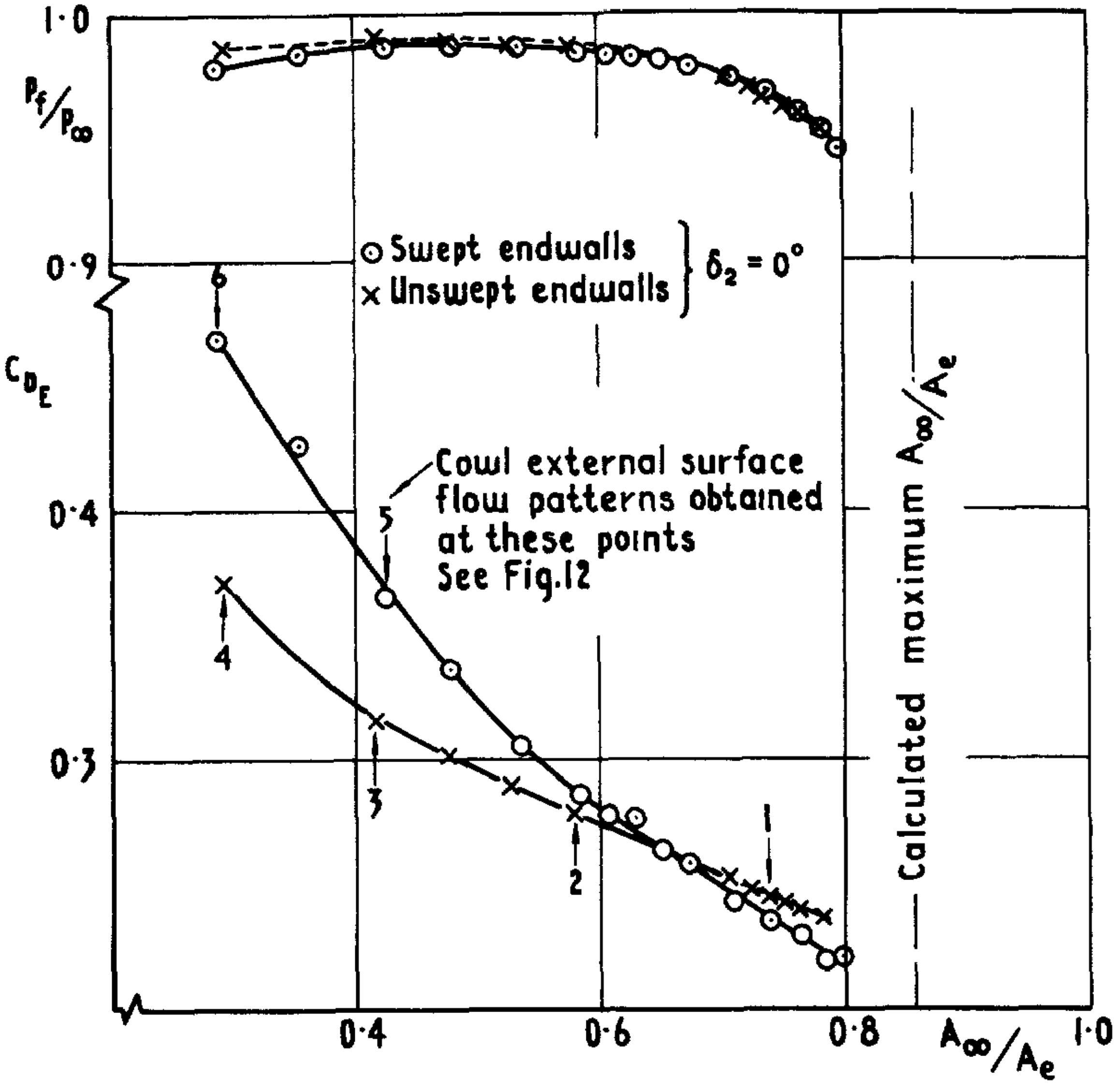

a $M_\infty = 0{\cdot}60$

Fig. 10 Variation of mean pressure recovery and external drag coefficient with mass flow ratio

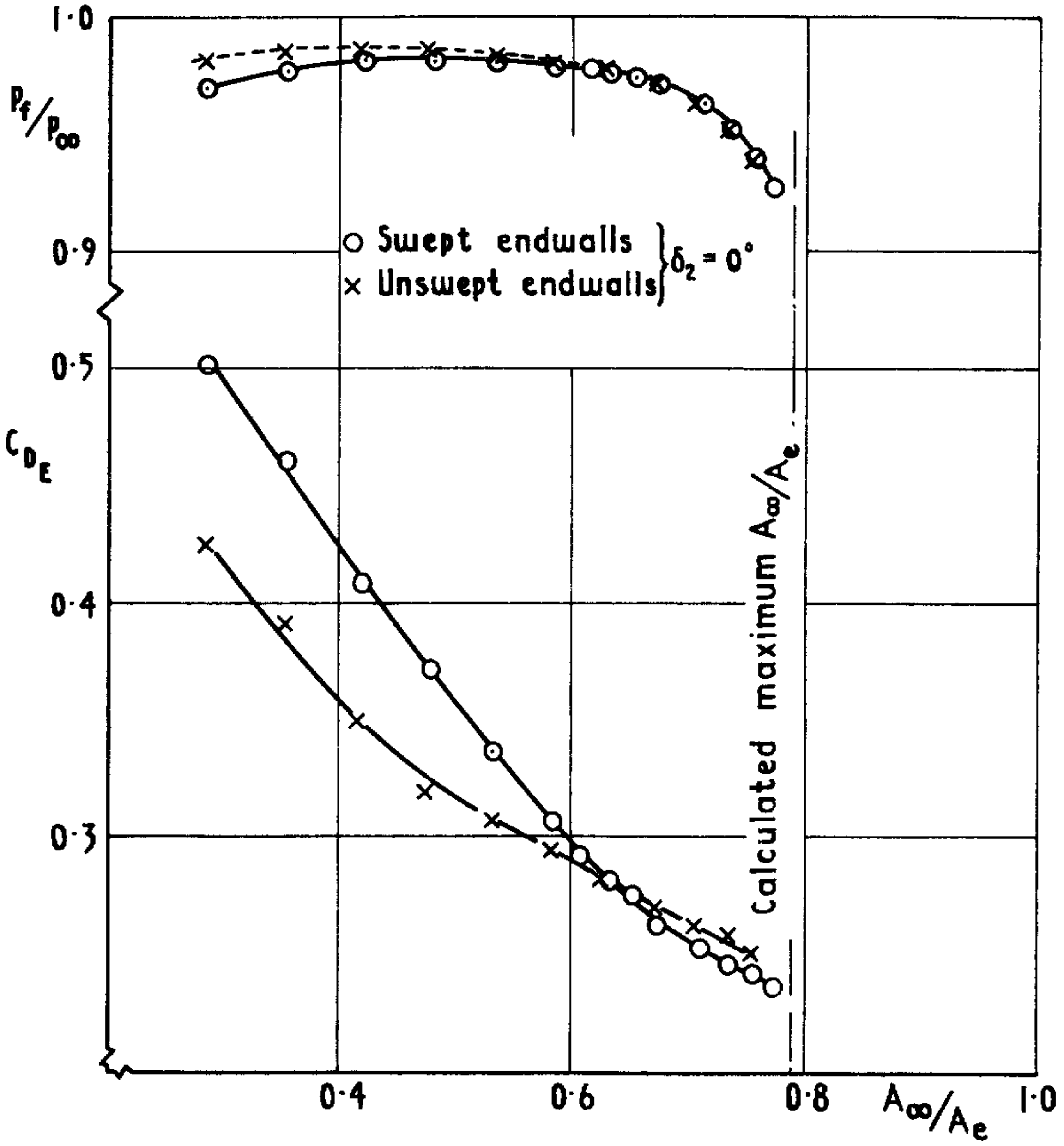

b $M_\infty = 0·70$

Fig. 10 contd

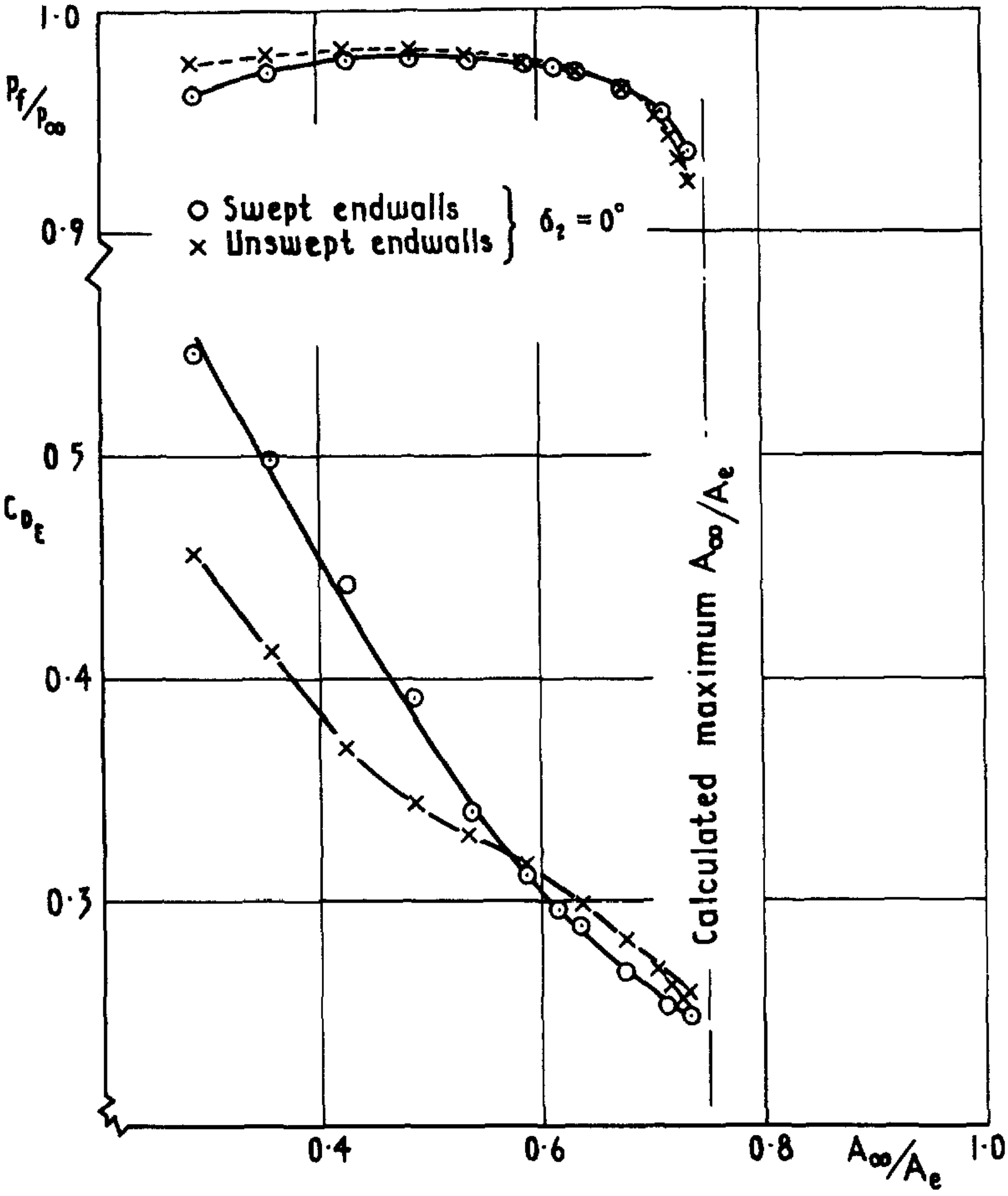

c $M_\infty = 0·80$

Fig.10 contd

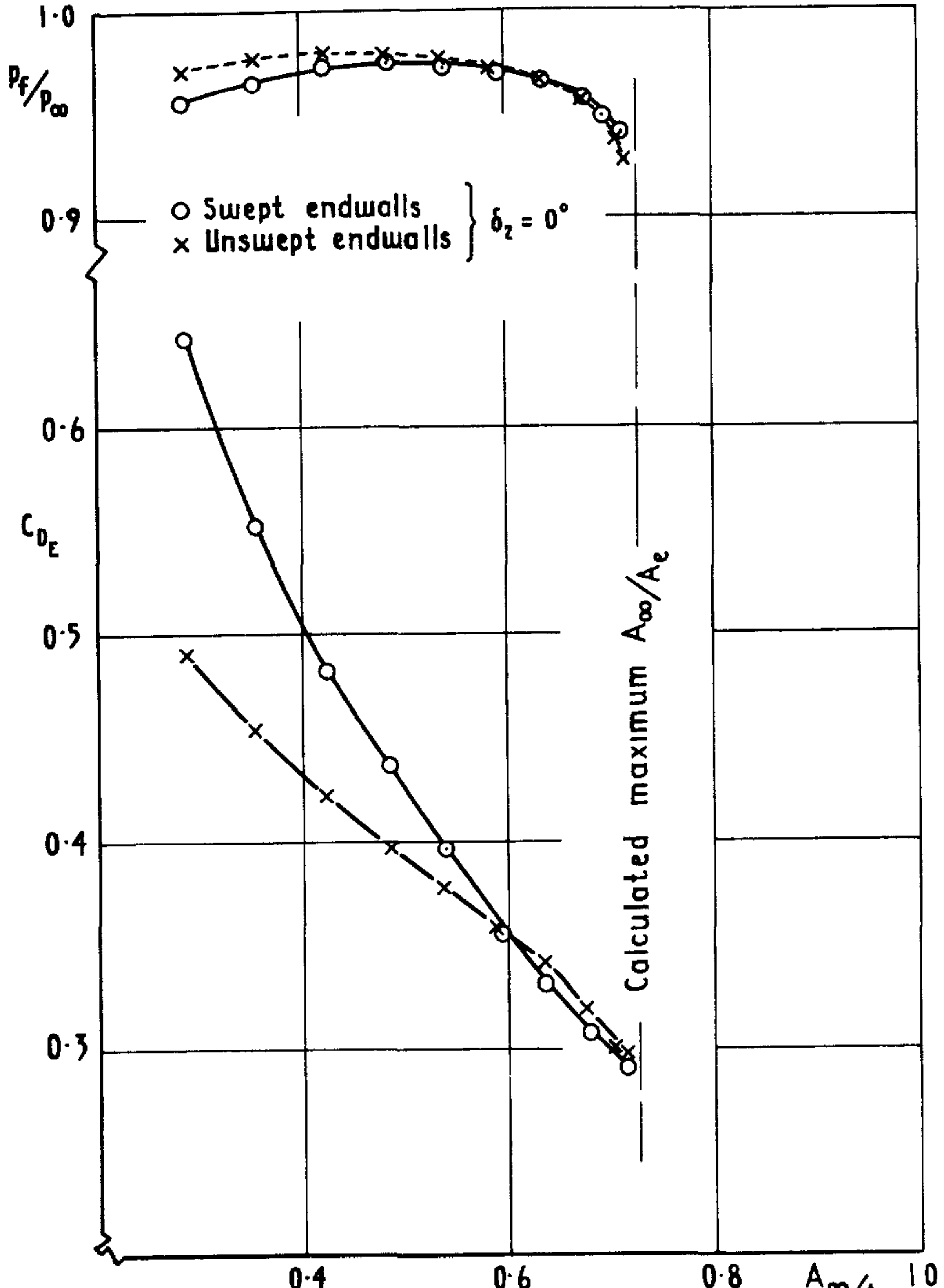

d $M_\infty = 0{\cdot}90$

Fig.10 contd

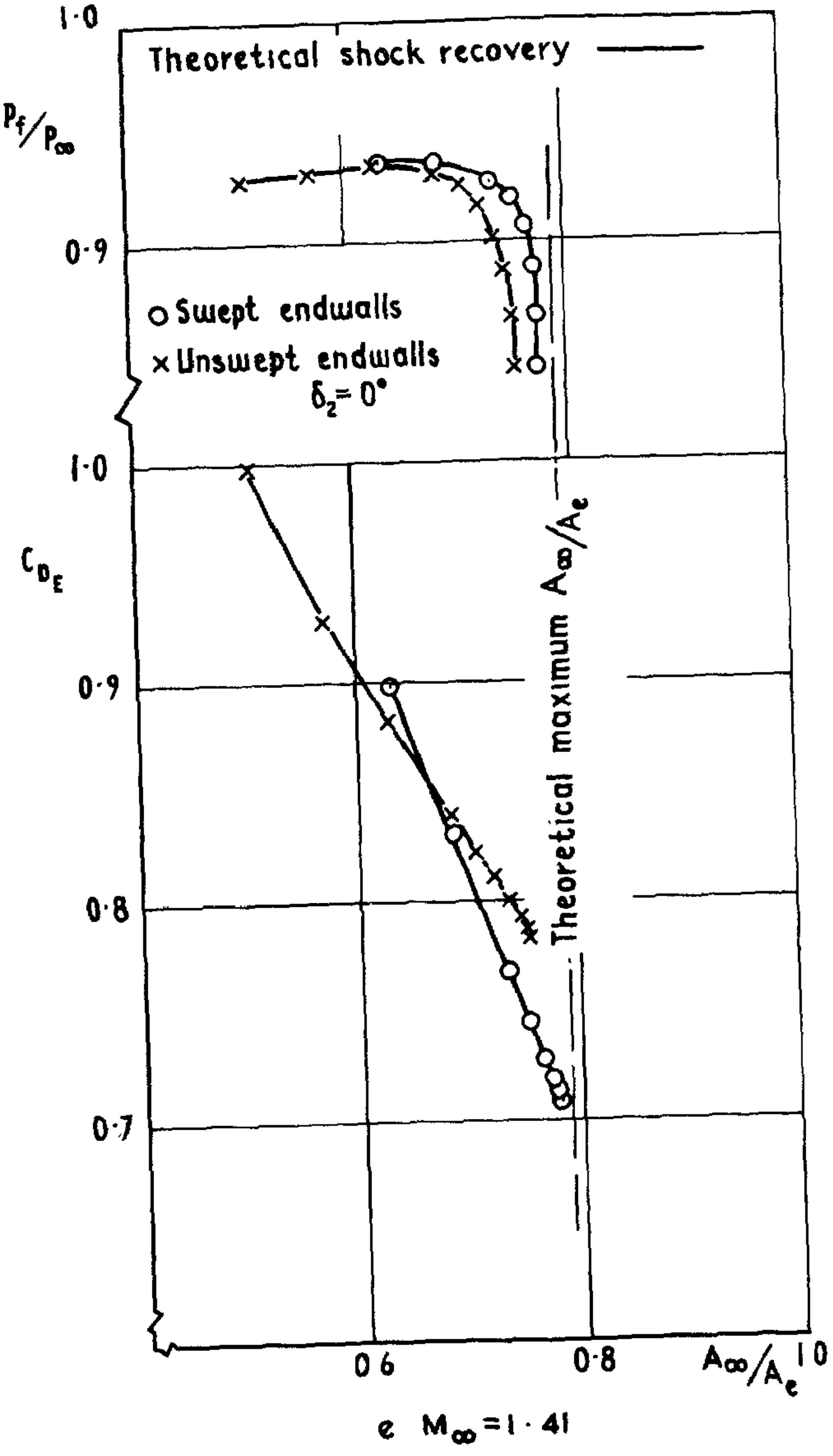
1·0
P_f/P_∞
Theoretical shock recovery
0·9
○ Swept endwalls
× Unswept endwalls
δ₂ = 0°
1·0
C_D_E
0·9
0·8
0·7
Theoretical maximum A∞/Ae
0·6
0·8
A∞/Ae
1·0
e M∞ = 1·41

Fig.10 contd

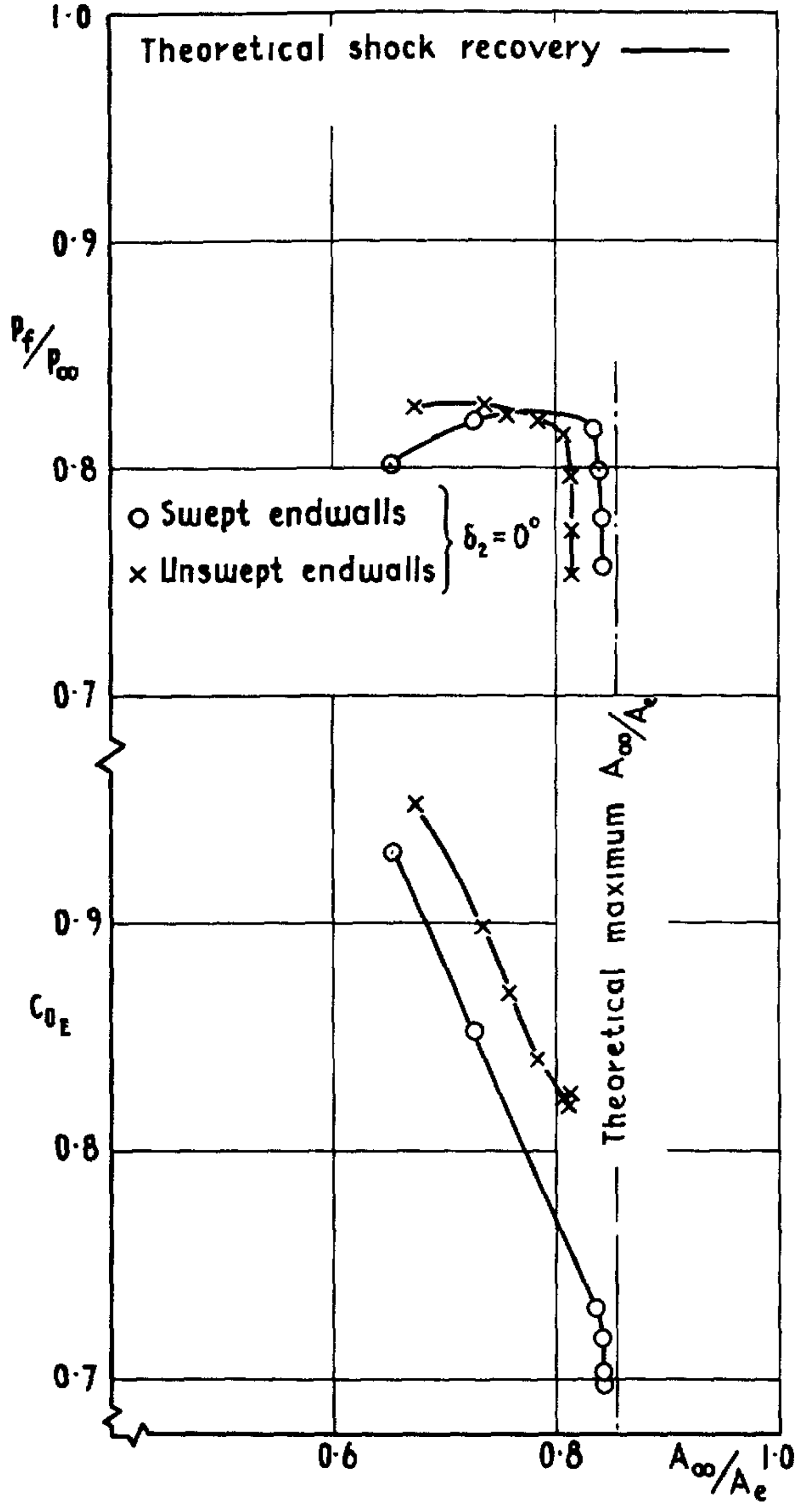

f $M_\infty = 1{\cdot}71$

Fig.10 contd

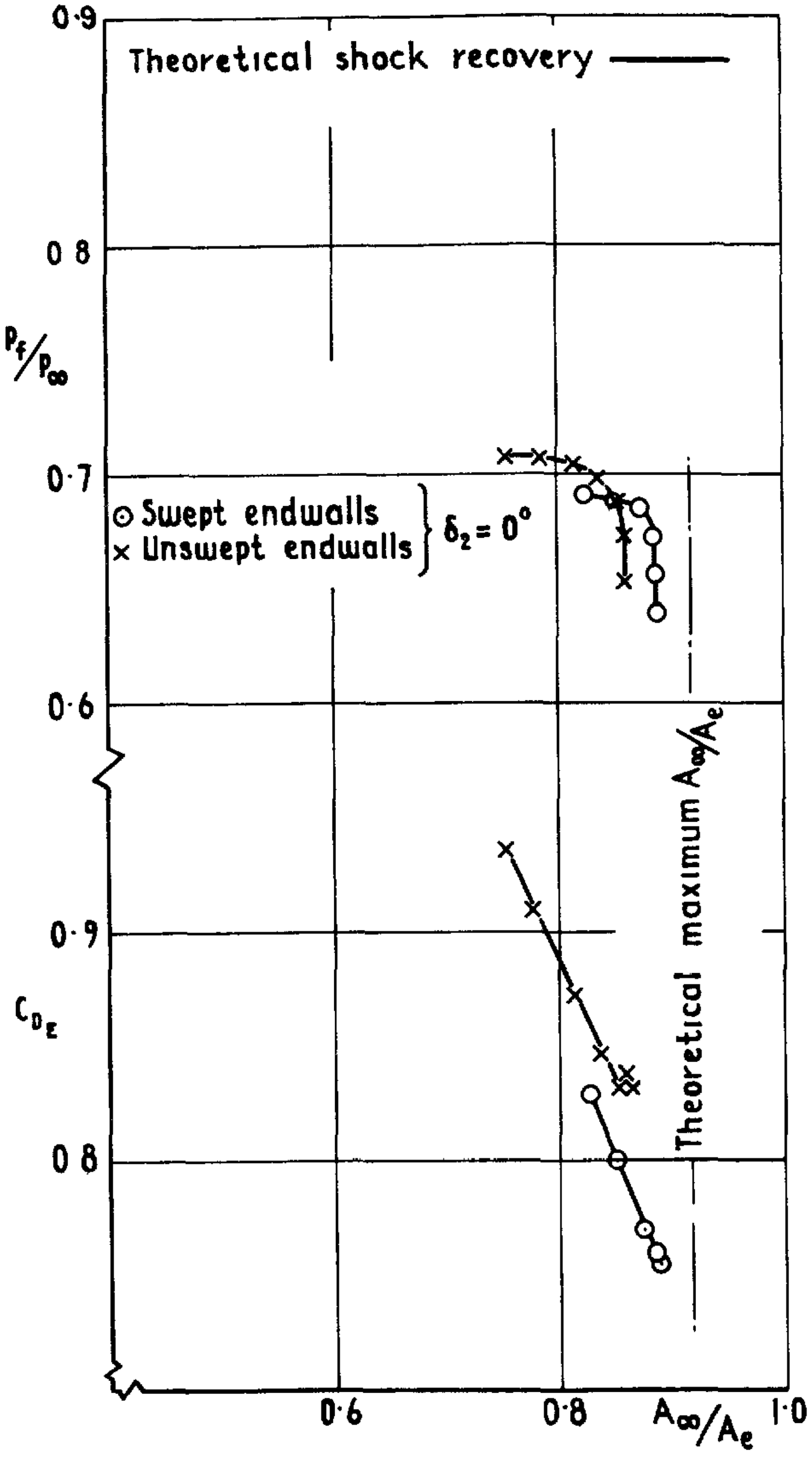

g $M_\infty = 2 \cdot 00$

Fig.10 concld

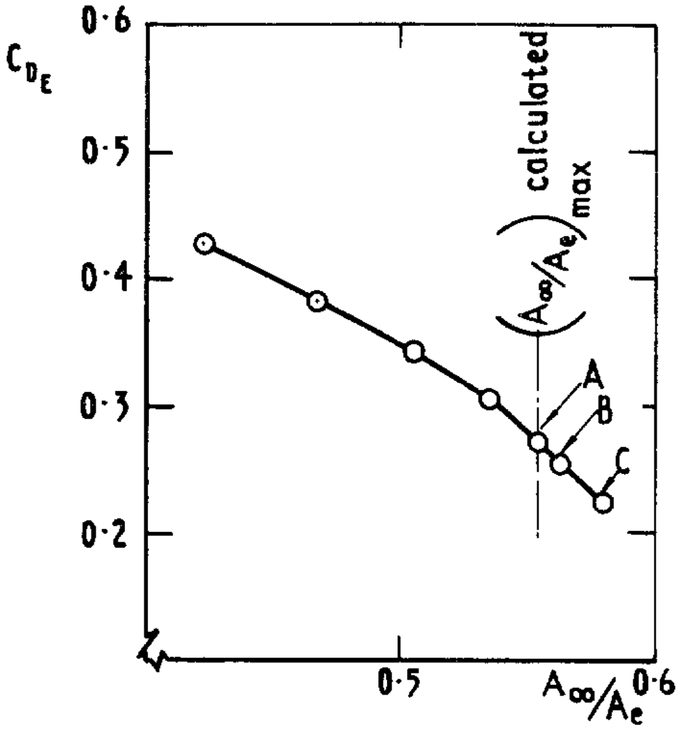

	A_∞/A_e	Measured C_{D_E}	Correction ΔC_{D_E}	Corrected C_{D_E}
Calculated maximum value	0·553	———	———	———
0·98 x cal^{cd} maximum value	0·542	0·295	0	0·295
Point A	0·553	0·273	0·022	0·295
Point B	0·562	0·253	0·040	0·293
Point C	0·580	0·224	0·076	0·300

Fig. 11 Illustrating correction applied to measurements at subsonic speed made when intake throat is choked

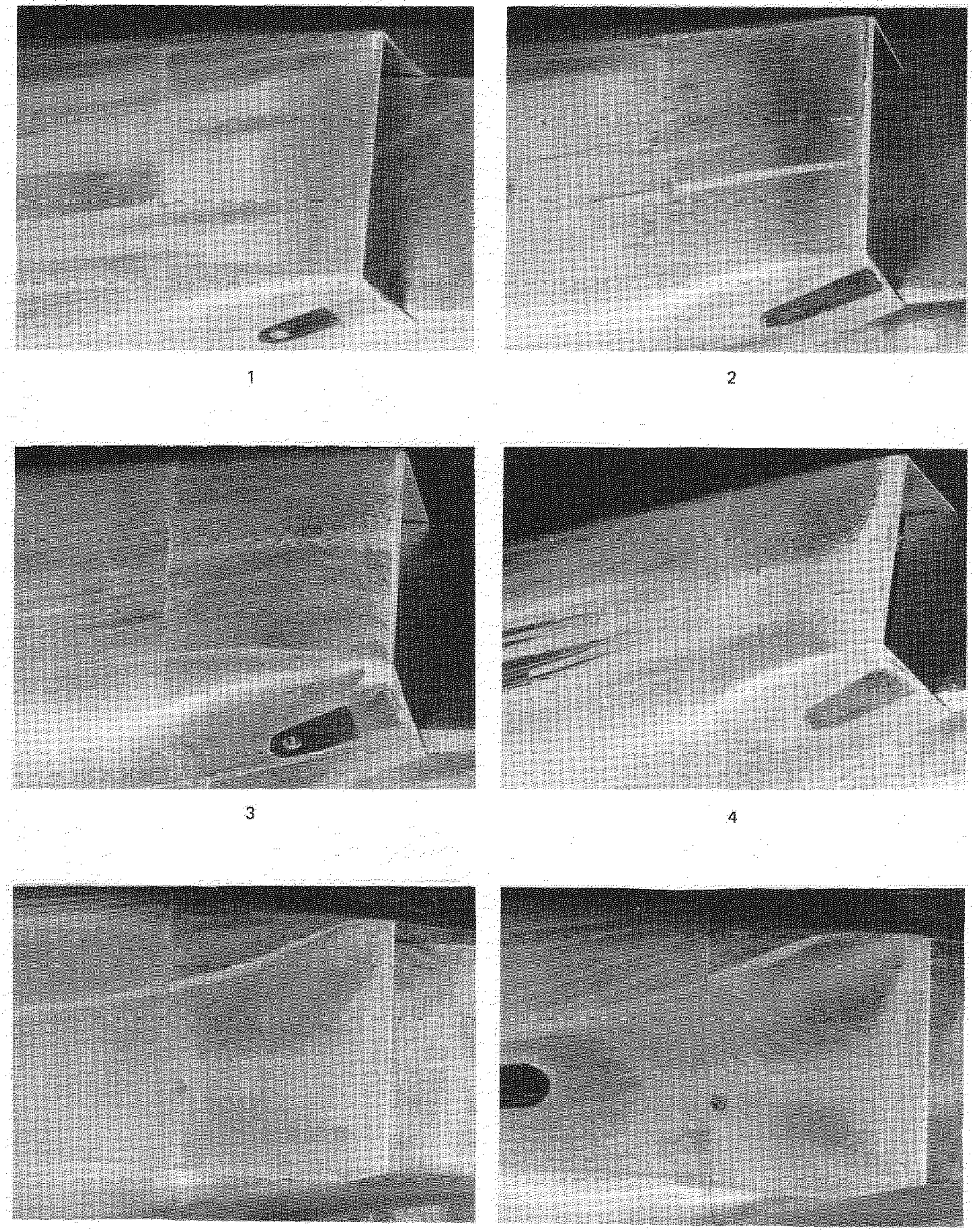

Fig.12 Characteristics of cowl external surface flow, $M_\infty = 0.60$

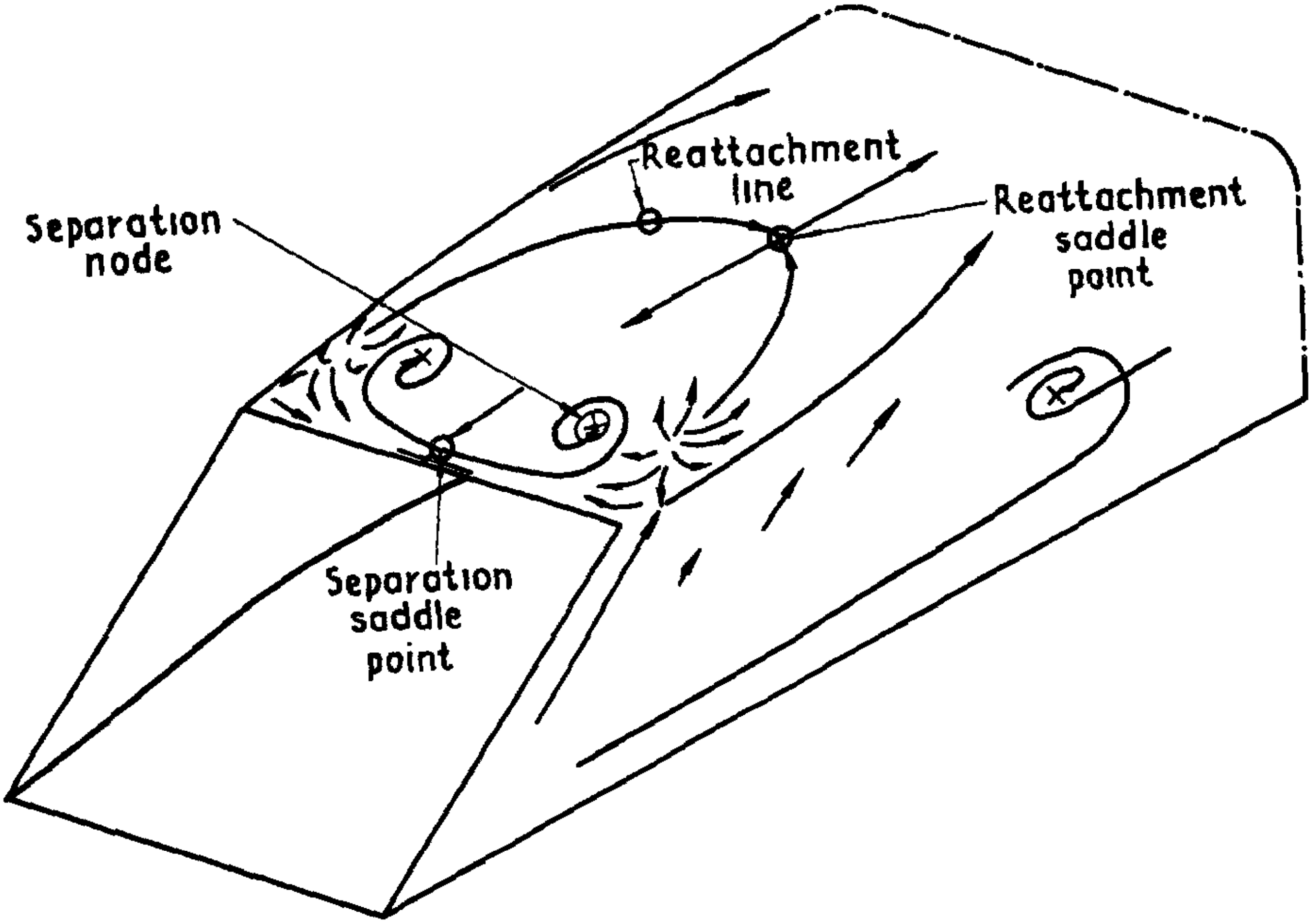

Fig.13 Schematic interpretation of cowl surface flow pattern

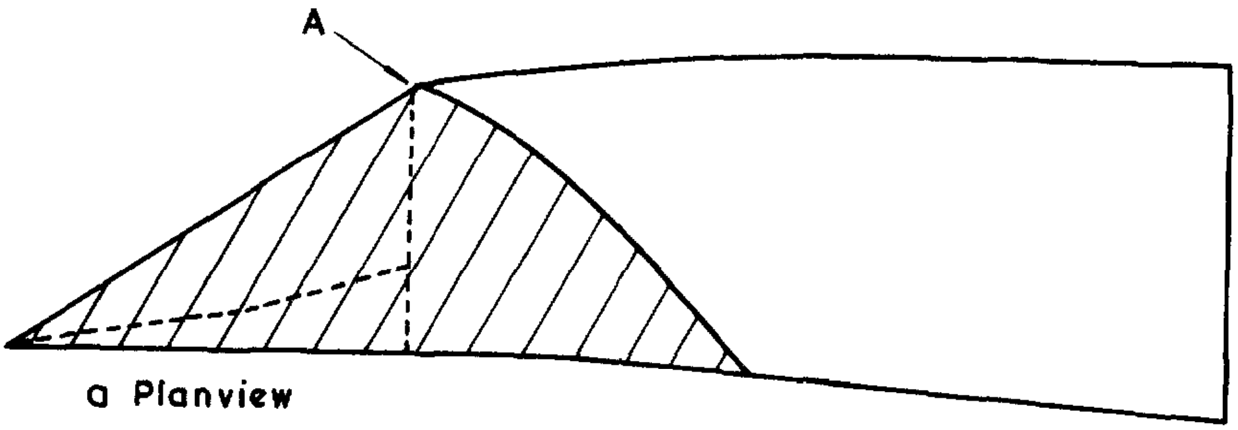

a Planview

Shaded regions show additional material required by the introduction of swept endwalls

Unswept endwalls t/c = 0·217
Swept endwalls t/c = 0·147

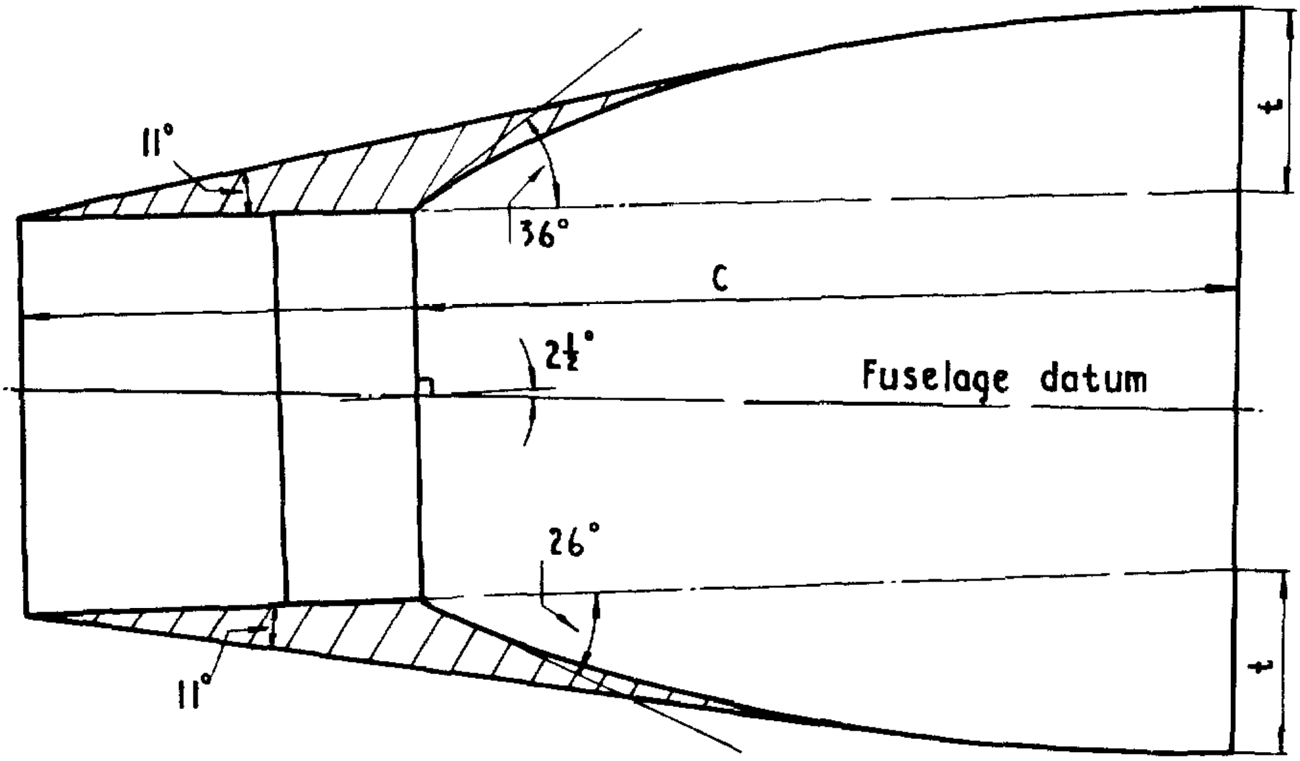

b Side elevation showing profiles of section close to the fuselage

Fig.14a & b Differences between configurations with swept and unswept endwalls

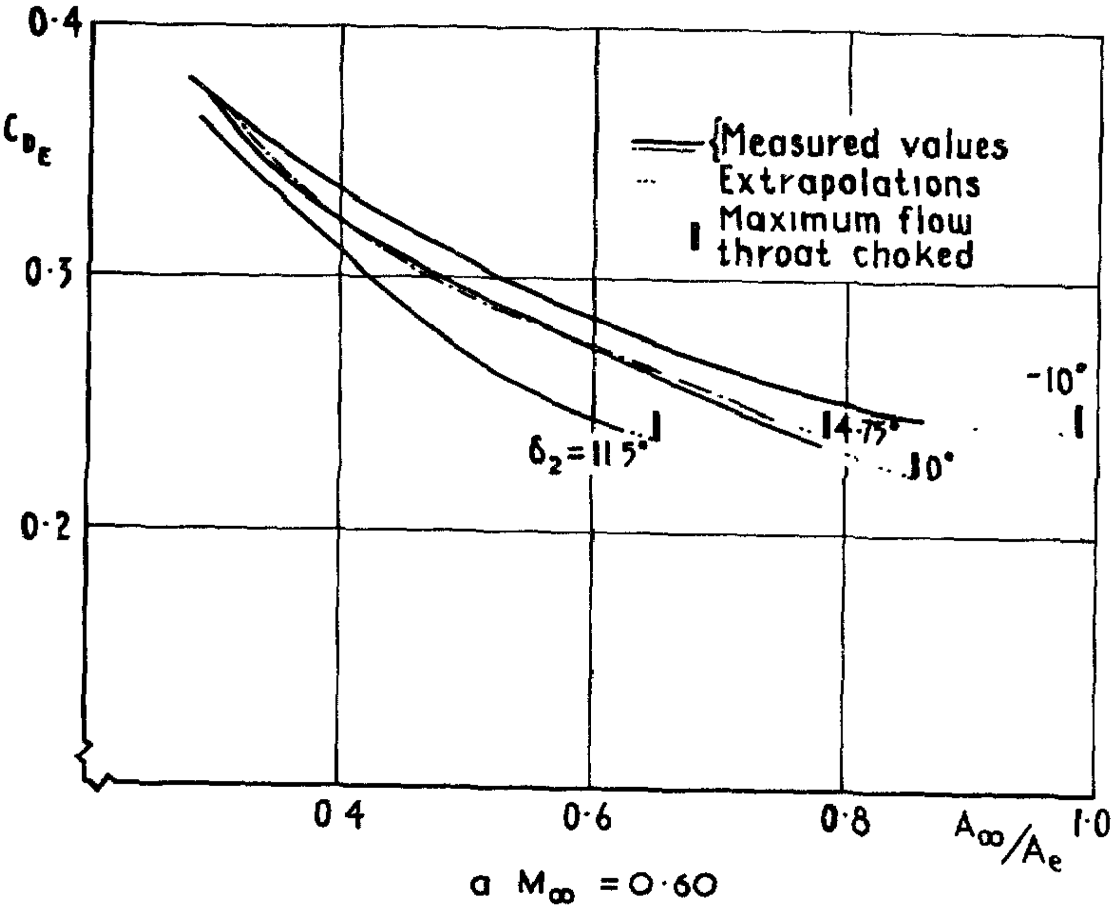

Fig.15 Effect of compression surface geometry on external drag at subsonic speeds. Intake with unswept endwalls

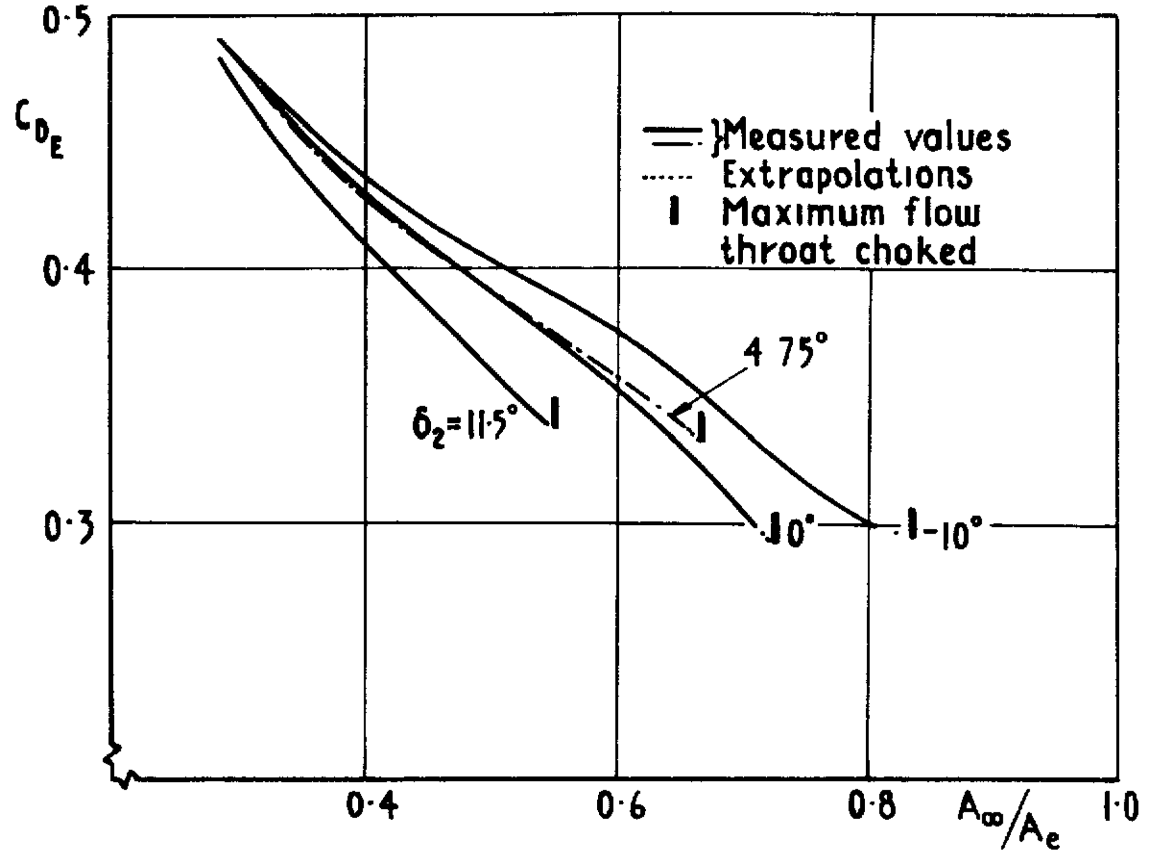

b $M_\infty = 0{\cdot}90$

Fig.15 contd

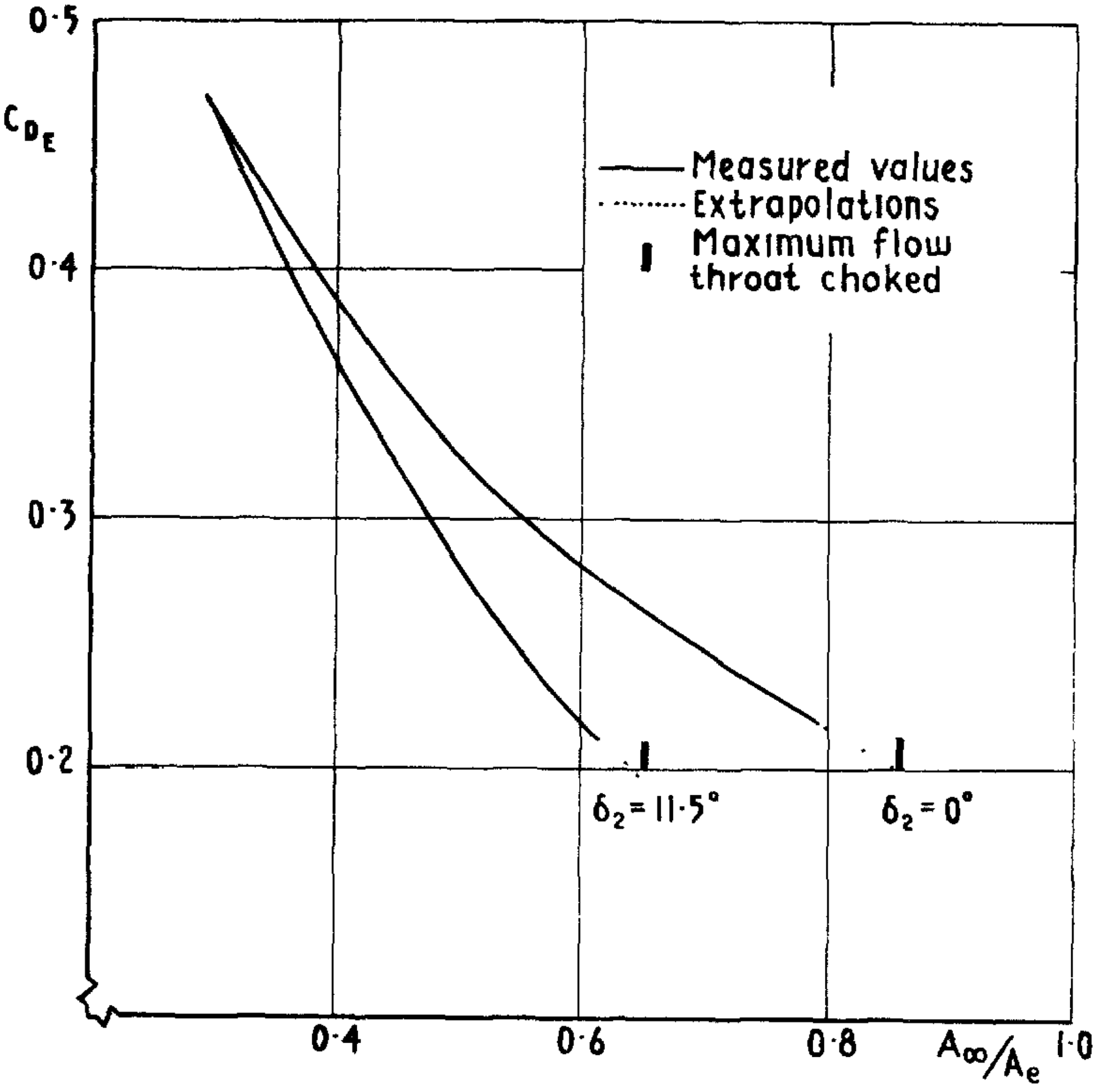

a $M_\infty = 0\ 60$

Fig.16 Effect of compression surface geometry on external drag at subsonic speeds. Intake with swept endwalls

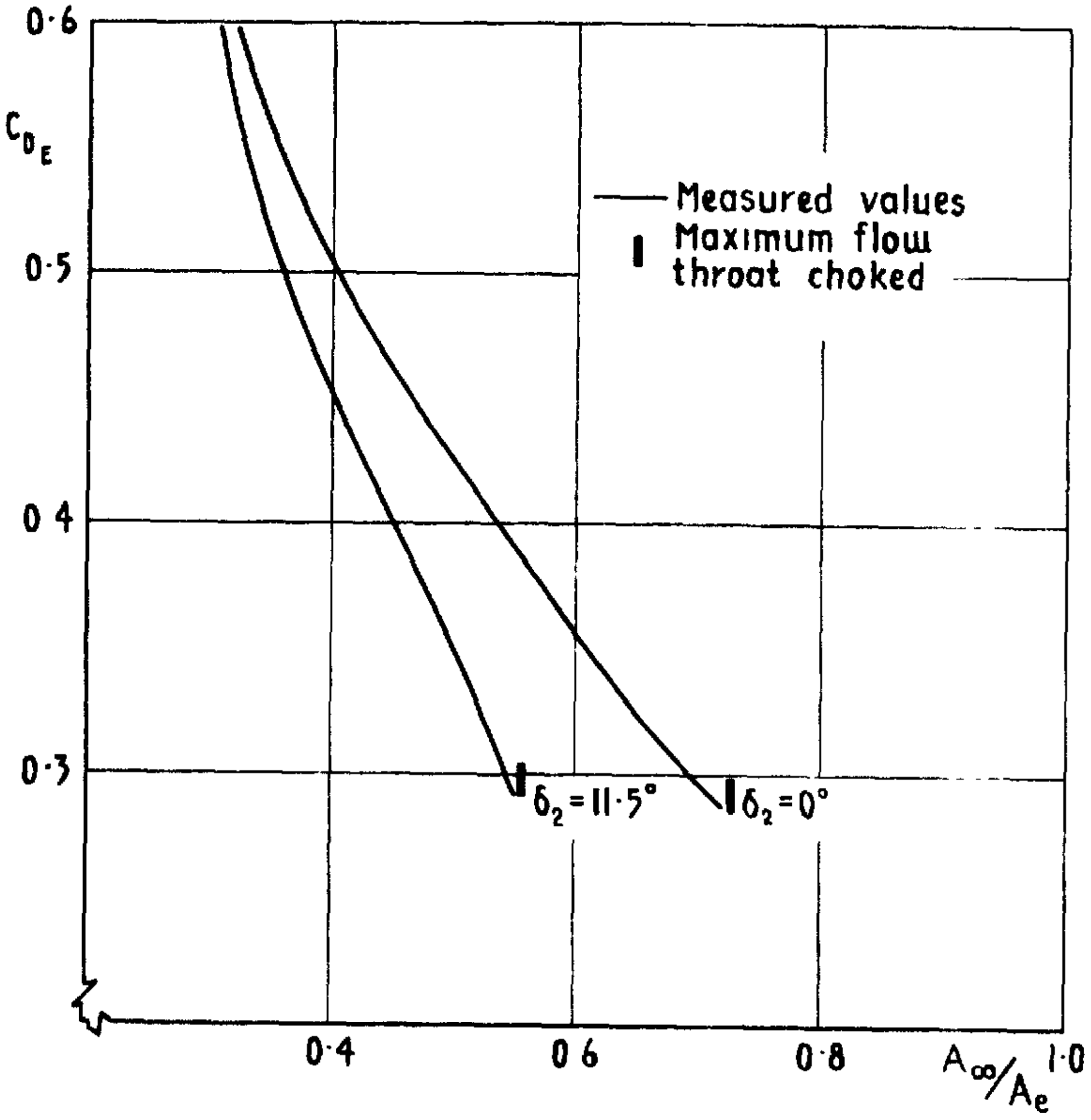

b $M_\infty = 0{\cdot}90$

Fig. 16 contd

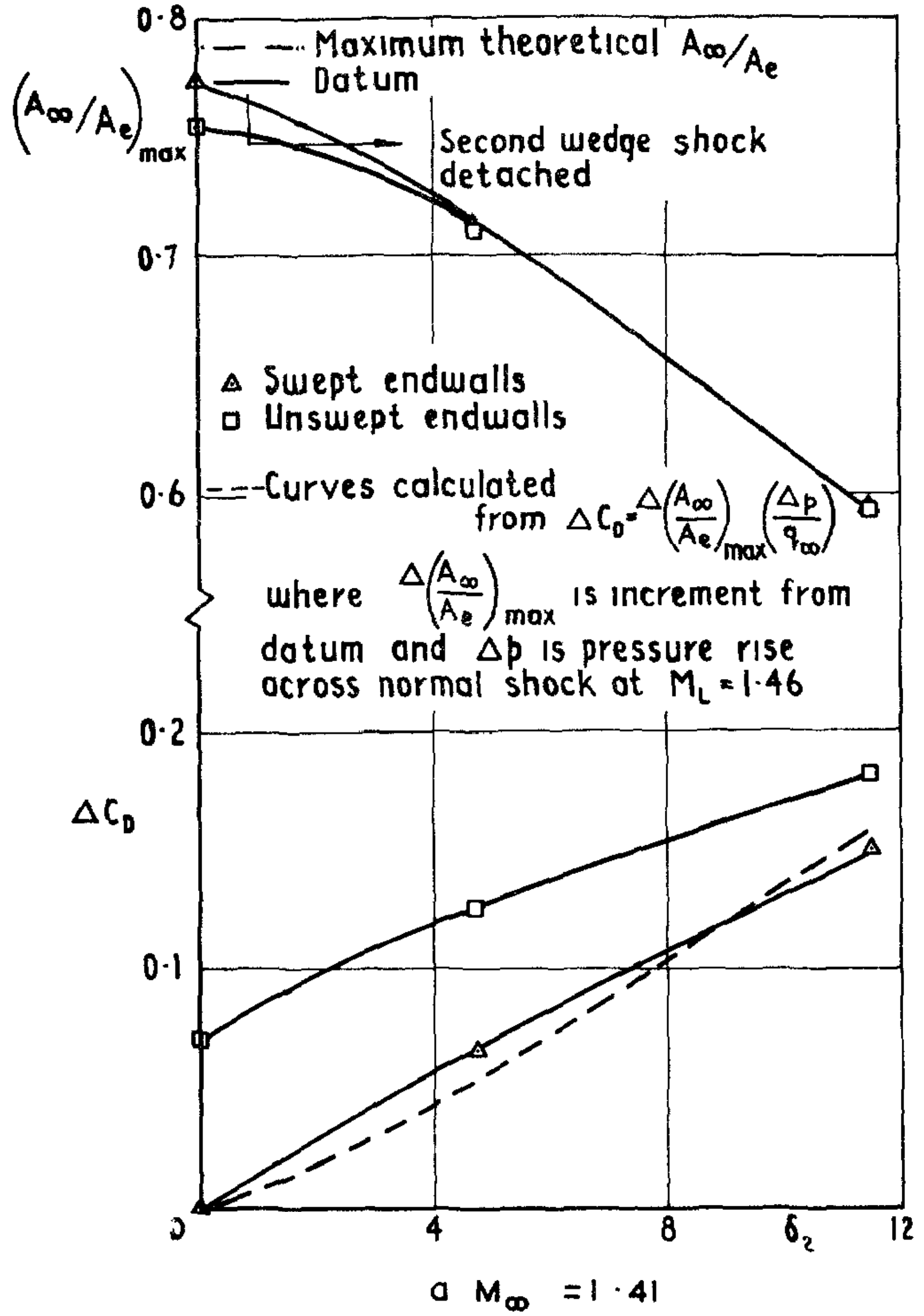

Fig. 17 Variation of maximum mass flow ratio and drag at this condition with compression surface geometry

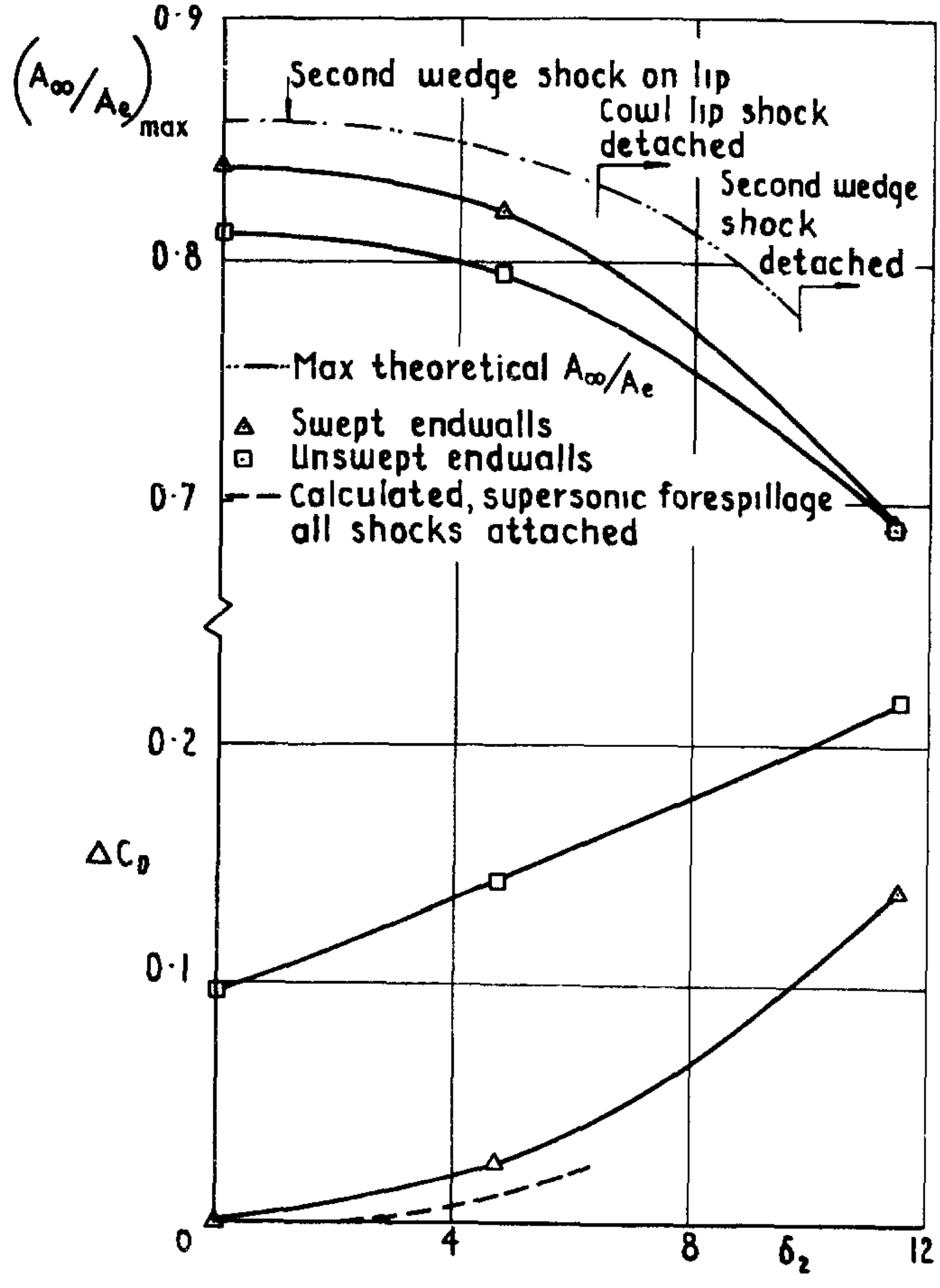

b $M_\infty = 1·71$

Fig.17 contd

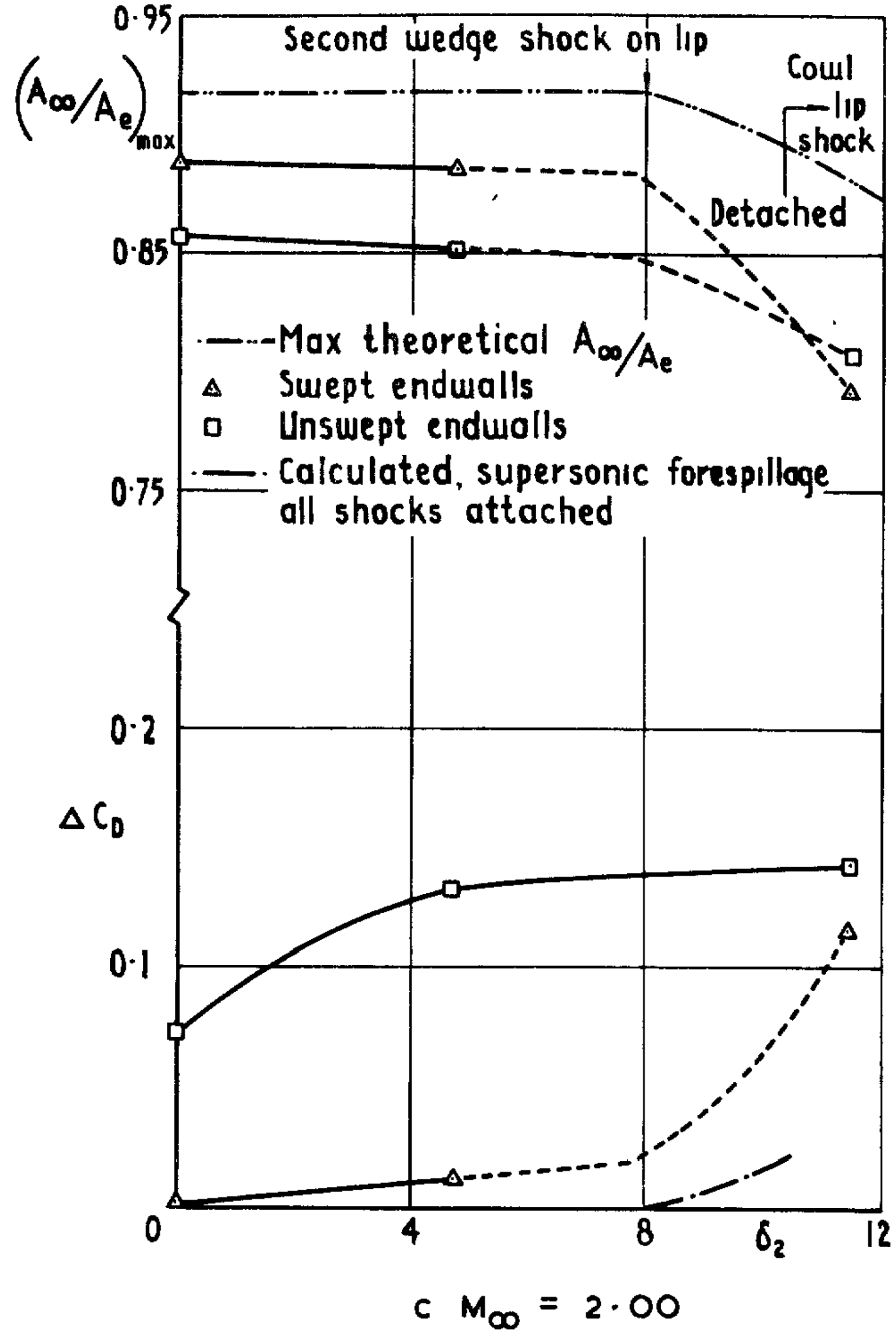

Fig. 17 concld

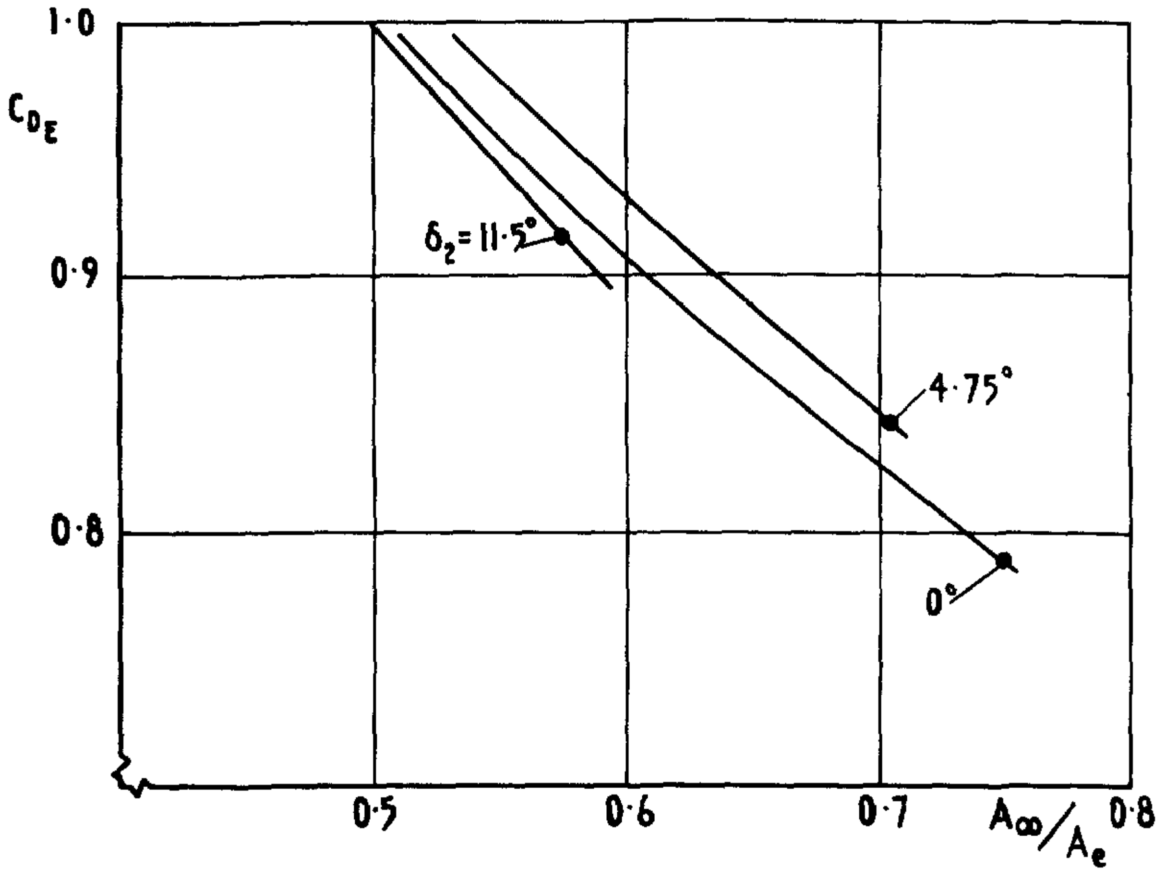

a $M_\infty = 1·41$

Fig.18 Spillage drag at supersonic speeds intake with unswept endwalls

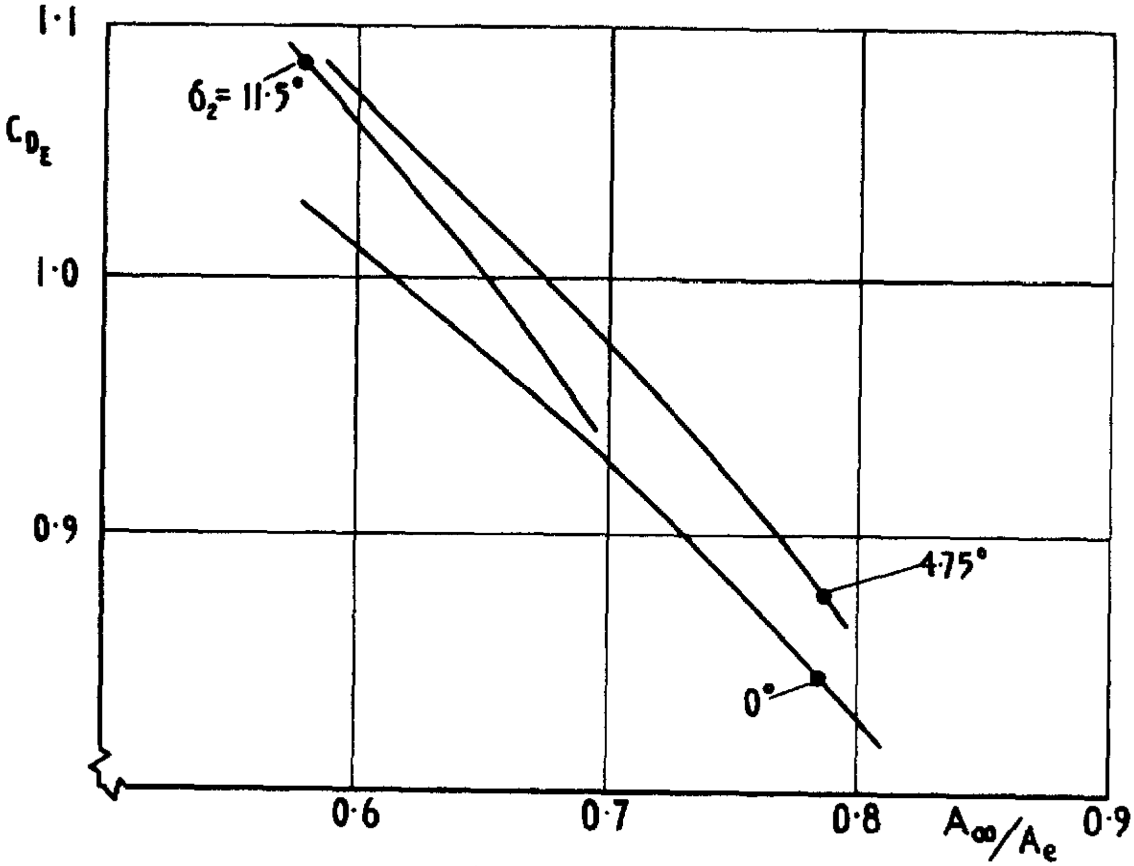

b $M_\infty = 1·71$

Fig.18 contd

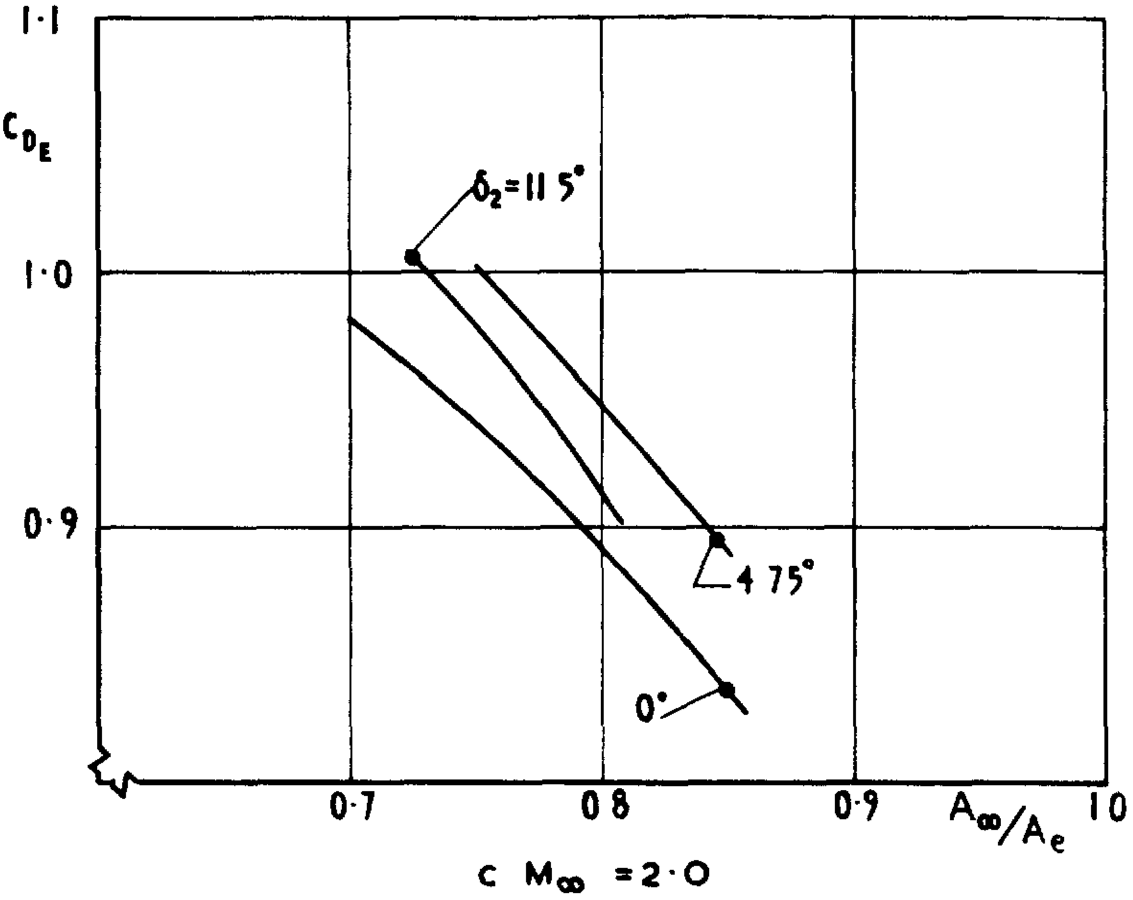

Fig 18 concld

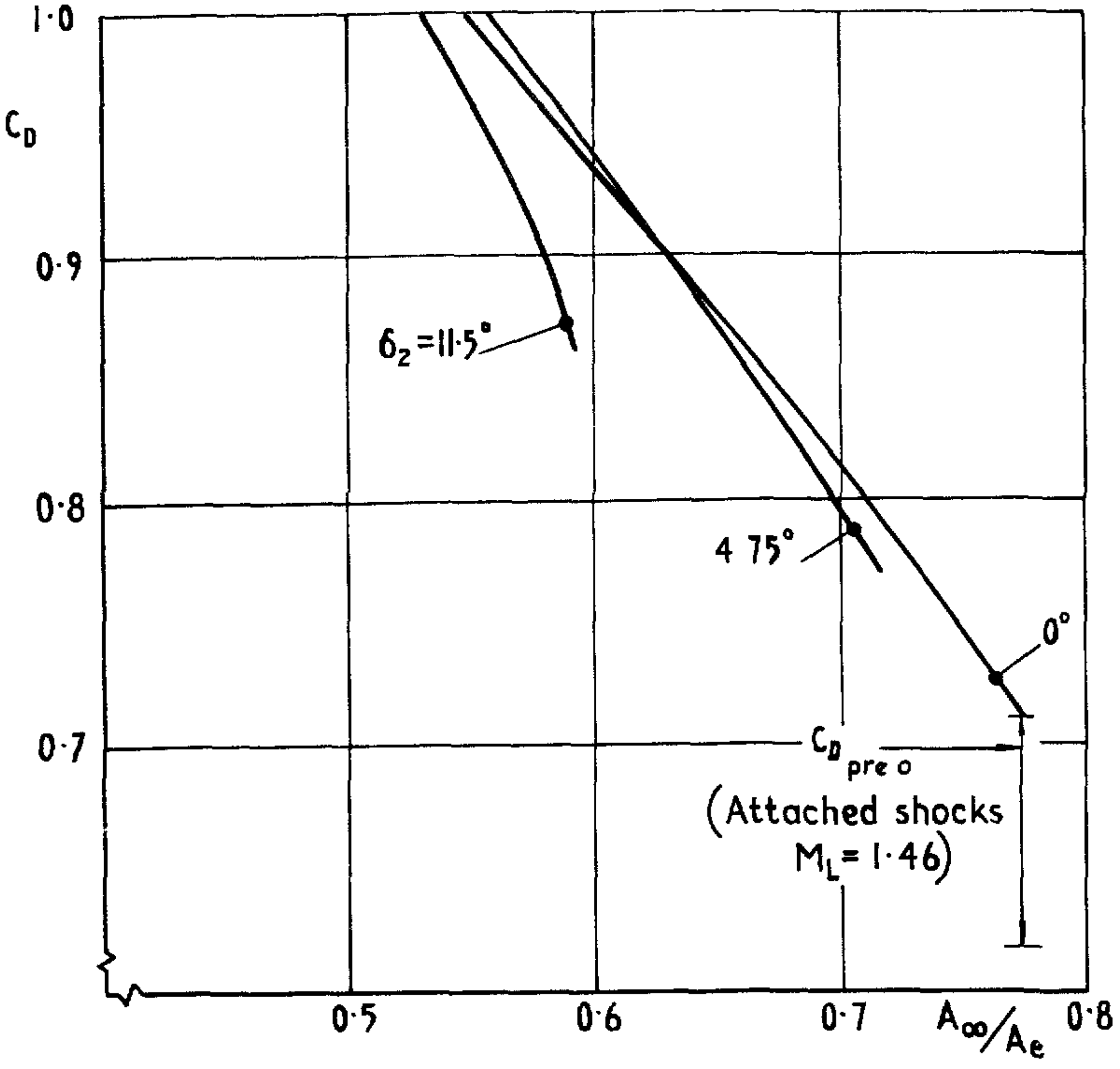

a $M_\infty = 1 \cdot 41$

Fig.19 Spillage drag at supersonic speeds intake with swept endwalls

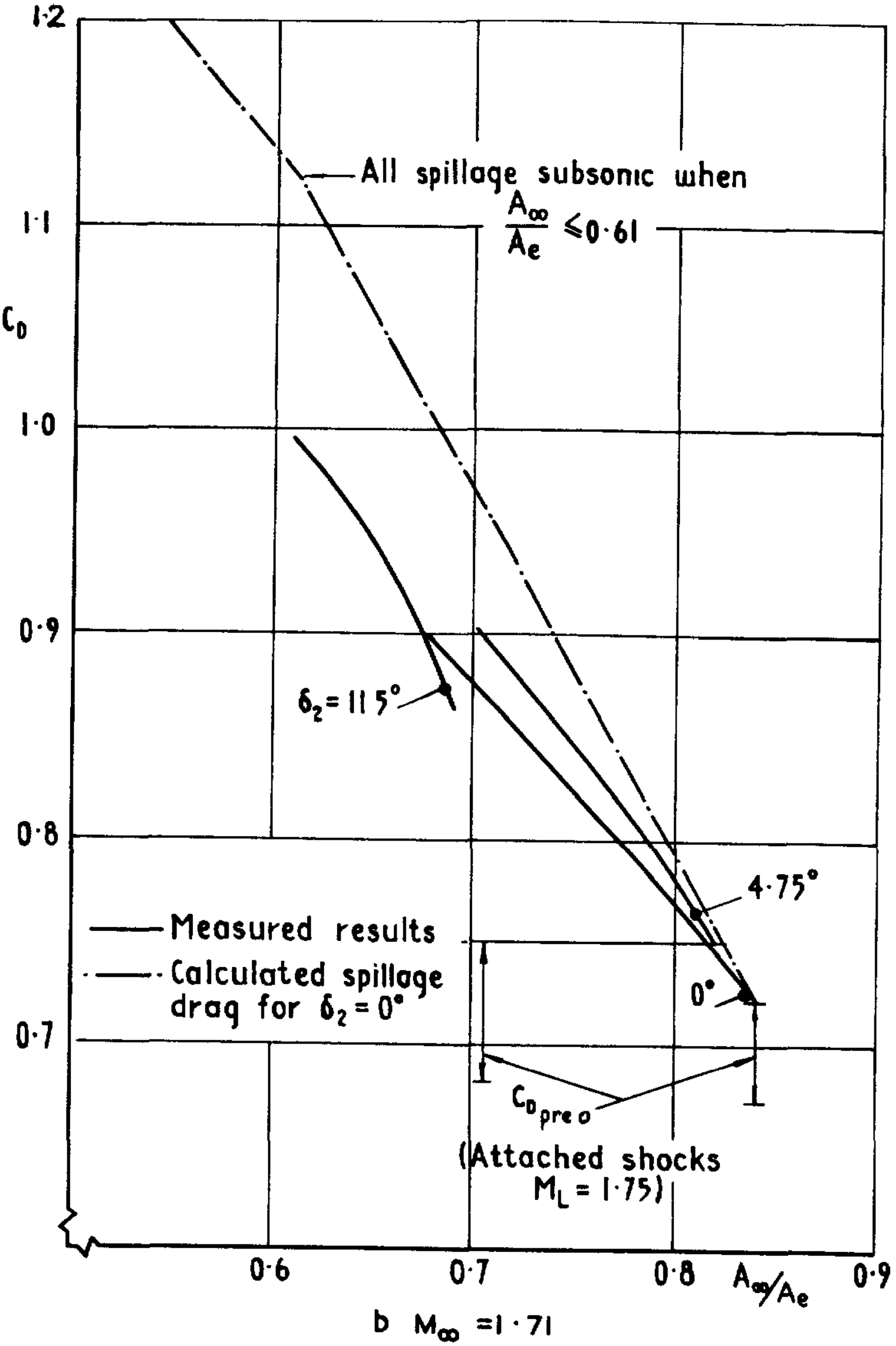

b $M_\infty = 1·71$

Fig.19 contd

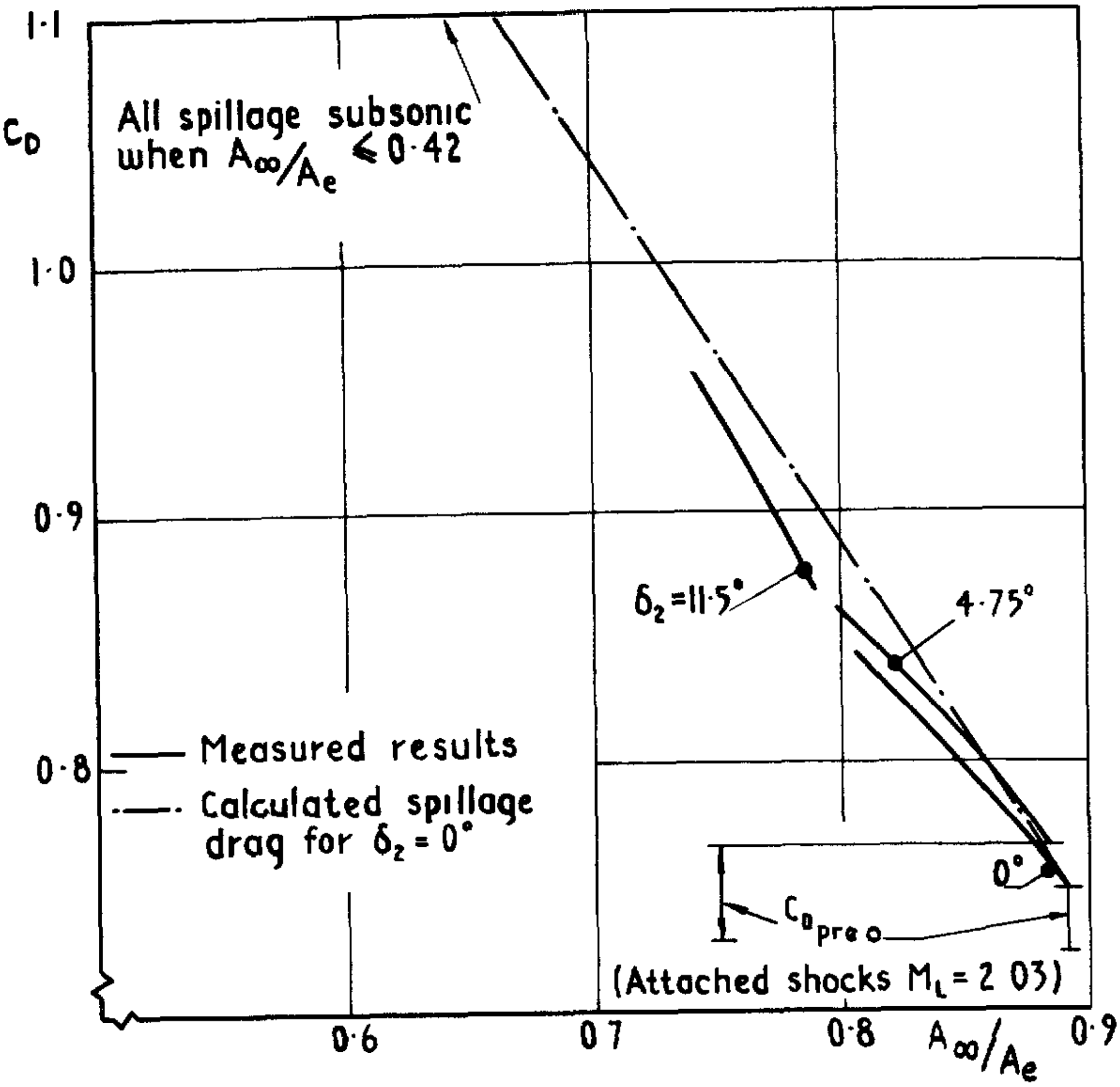

c $M_\infty = 2{\cdot}00$

Fig. 19 concld

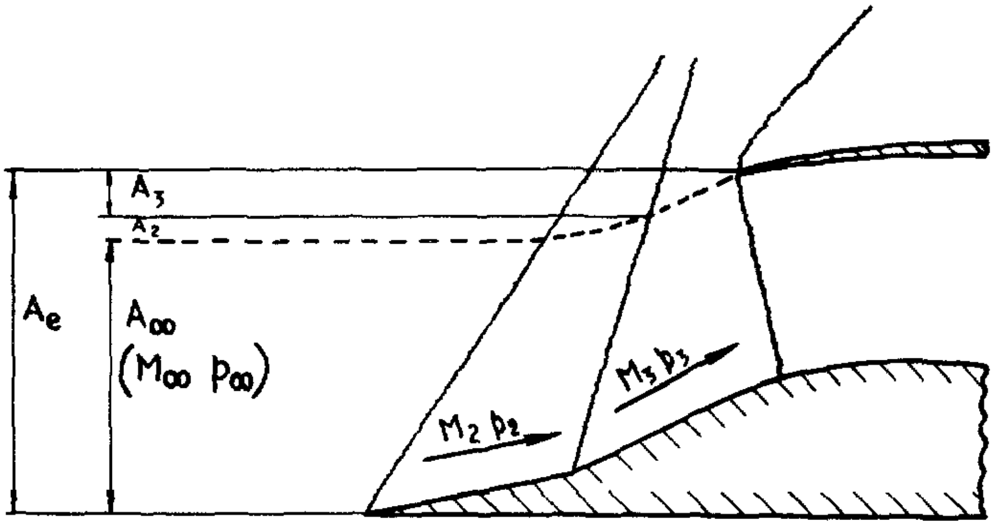

a Supersonic spillage

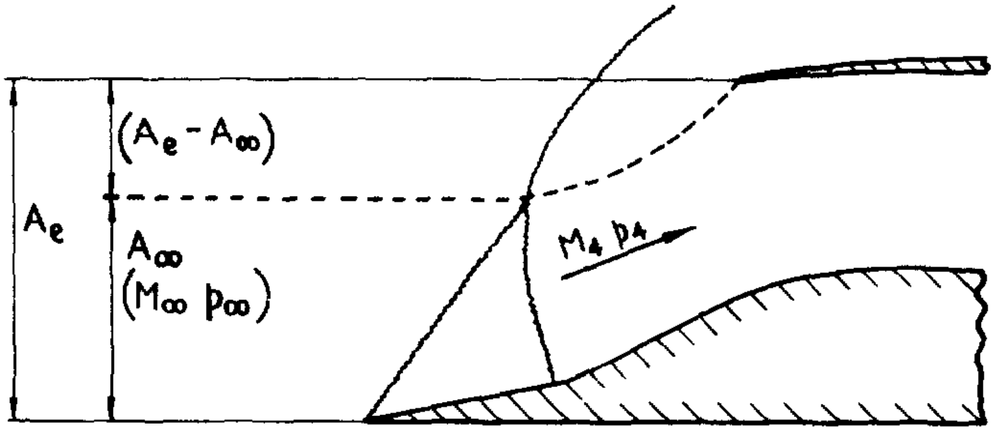

b Subsonic spillage

Fig.20a&b Shock geometries for particular flow spillage conditions

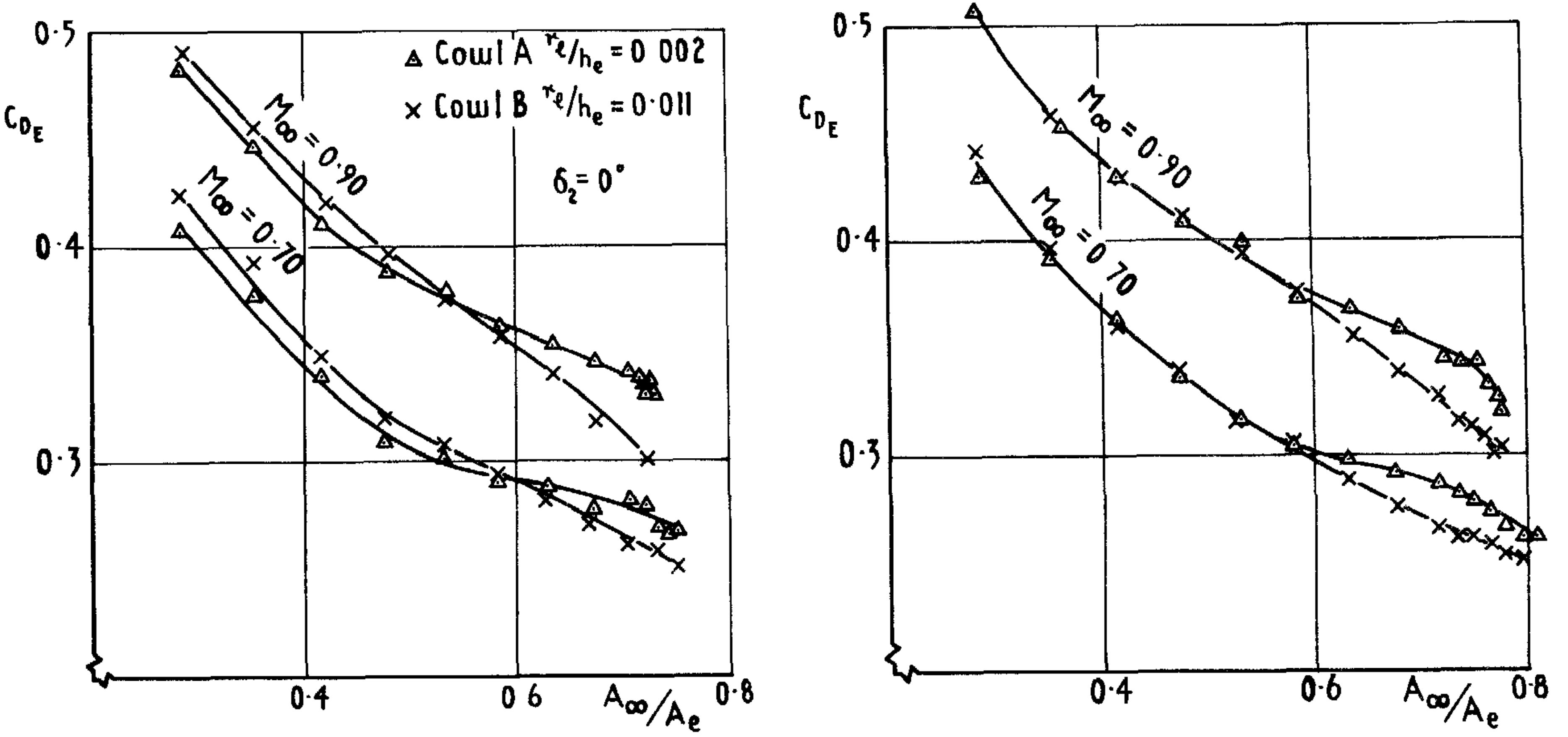

a Intake 1

b Intake 2

Fig.21a&b External drag curves showing effect of cowl lip radius

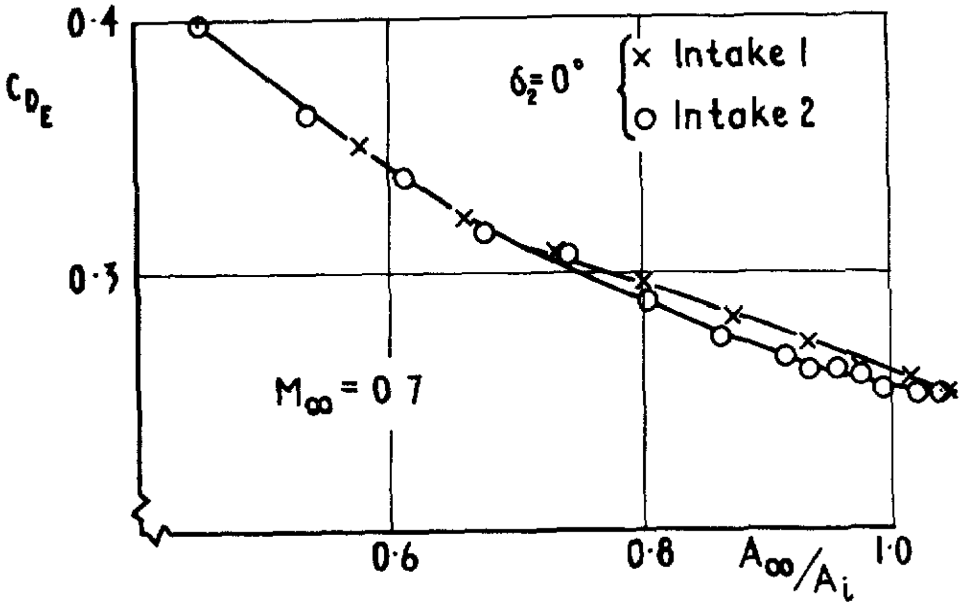

Fig.22 External drag as a function of inlet mass flow ratio

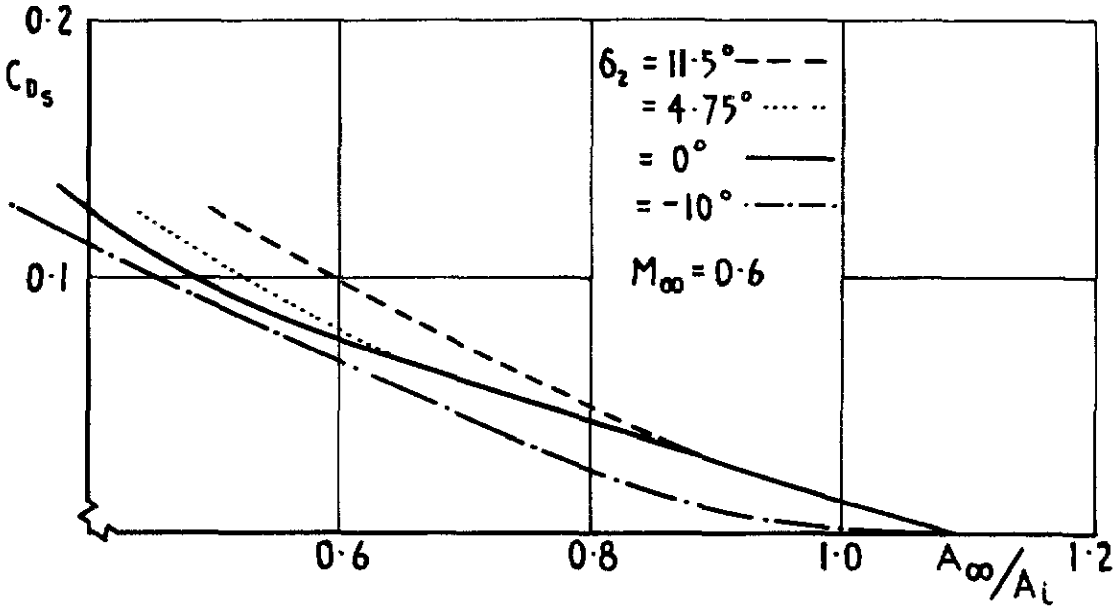

Fig.23 Spillage drag as a function of inlet mass flow ratio - variation with compression surface geometry

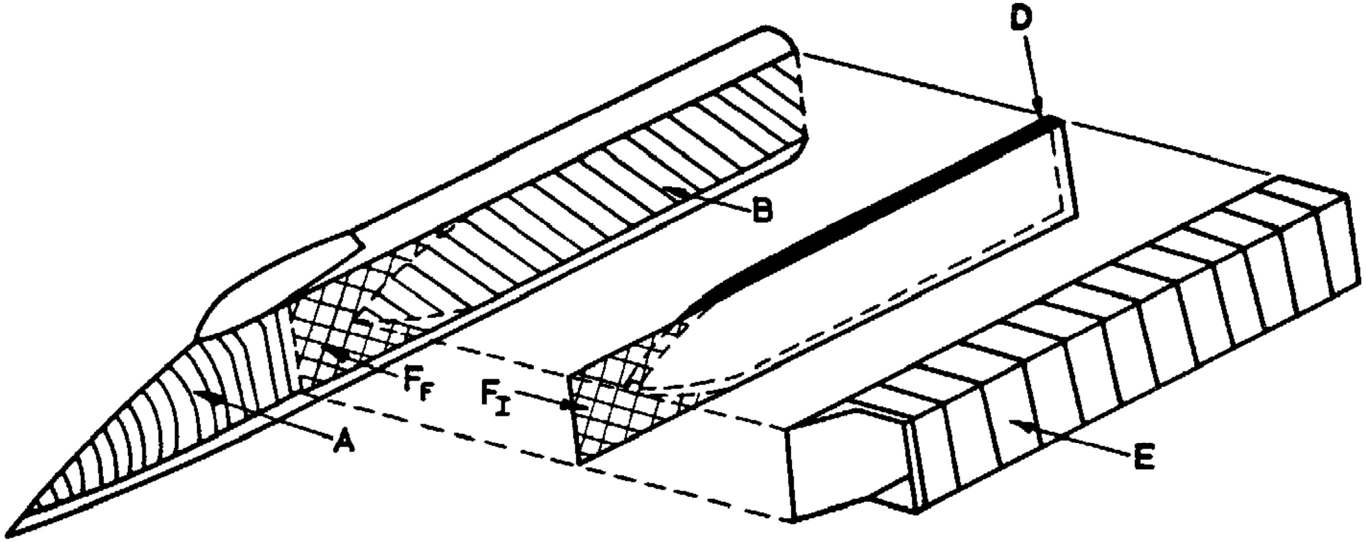

Fig. 24 Surface areas for skin friction estimation for diverter and installation drag analyses

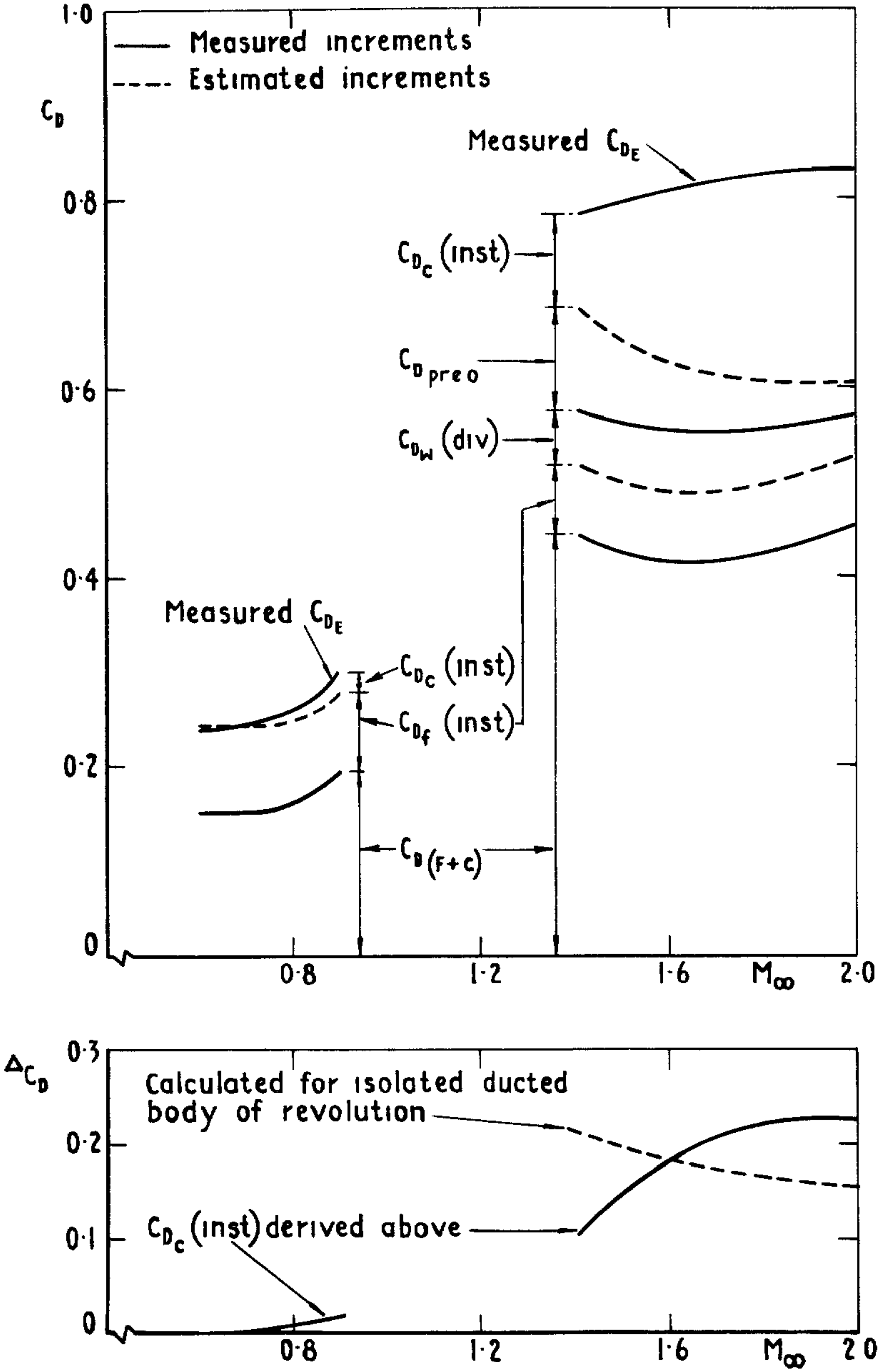

Fig.25 Incremental drag analysis (see Table 5)

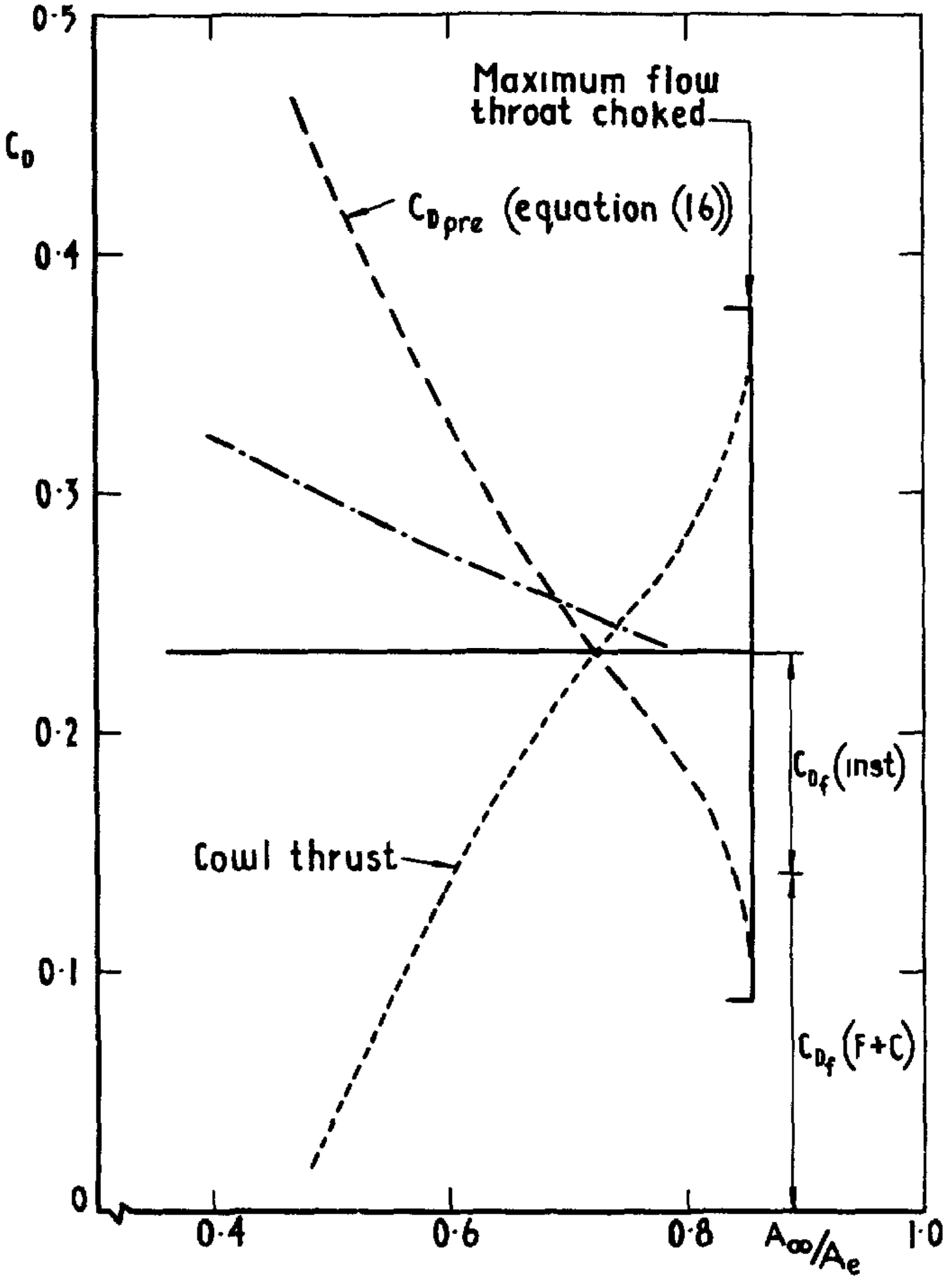

a $M_\infty = 0·60$

Fig.26 Comparison of calculated and measured values of drag

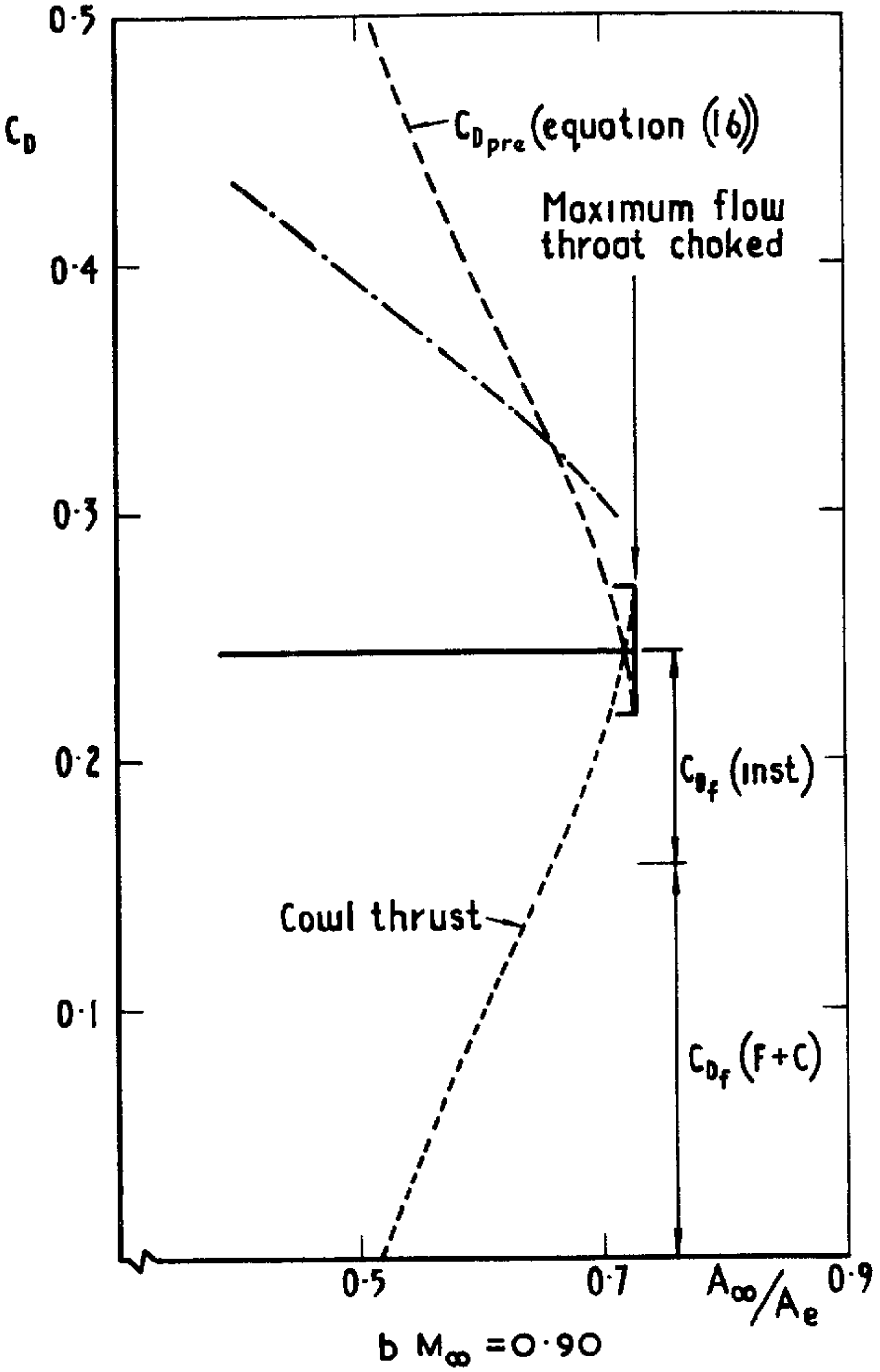

b $M_\infty = 0·90$

Fig.26 contd

Printed in England for Her Majesty's Stationery Office by Royal Aircraft Establishment, Farnborough Dd 505716 K4 11/73

ARC CP No.1269
October 1972

533 697 24
533 6 013 12
533.6 013 122

Dobson, M D

THE EXTERNAL DRAG OF FUSELAGE SIDE INTAKES
RECTANGULAR INTAKES WITH COMPRESSION SURFACES
VERTICAL

An experiment designed to measure the external drag of fuselage side intakes is described The scope of the experiment and the techniques employed are discussed and an assessment is made of the accuracy of results

Measurements of the external drag of rectangular intakes installed on the sides of a fuselage are presented Results at subsonic speeds show that drag at full flow is independent of compression surface geometry, so that substantial flow spillage may be achieved for little drag penalty provided that the intake throat Mach number is kept high by elevation of the compression surface For a given total turning of the flow by the compression surface, spillage drag is found to be uniquely related to the inlet mass flow ratio (as distinct from capture mass flow ratio) Radius of the cowl lip is found to affect the drag of the intake at full flow but becomes less important as flow is reduced Drag at full flow for intakes with swept end walls is lower than for a configuration in which they are unswept but the spillage drag rise is greater

(Over)

These abstract cards are inserted in Technical Reports for the convenience of Librarians and others who need to maintain an Information Index

Cut here

ARC CP No 1269
October 1972

533 697 24
533 6 013 12
533 6 013 122

Dobson, M D

THE EXTERNAL DRAG OF FUSELAGE SIDE INTAKES
RECTANGULAR INTAKES WITH COMPRESSION SURFACES
VERTICAL

An experiment designed to measure the external drag of fuselage side intakes is described The scope of the experiment and the techniques employed are discussed and an assessment is made of the accuracy of results

Measurements of the external drag of rectangular intakes installed on the sides of a fuselage are presented Results at subsonic speeds show that drag at full flow is independent of compression surface geometry, so that substantial flow spillage may be achieved for little drag penalty provided that the intake throat Mach number is kept high by elevation of the compression surface For a given total turning of the flow by the compression surface, spillage drag is found to be uniquely related to the inlet mass flow ratio (as distinct from capture mass flow ratio) Radius of the cowl lip is found to affect the drag of the intake at full flow but becomes less important as flow is reduced Drag at full flow for intakes with swept end walls is lower than for a configuration in which they are unswept but the spillage drag rise is greater

(Over)

ARC CP No 1269
October 1972

533 697 24
533 6 013 12
533 6 013 122

Dobson, M D

THE EXTERNAL DRAG OF FUSELAGE SIDE INTAKES
RECTANGULAR INTAKES WITH COMPRESSION SURFACES
VERTICAL

An experiment designed to measure the external drag of fuselage side intakes is described. The scope of the experiment and the techniques employed are discussed and an assessment is made of the accuracy of results.

Measurements of the external drag of rectangular intakes installed on the sides of a fuselage are presented. Results at subsonic speeds show that drag at full flow is independent of compression surface geometry, so that substantial flow spillage may be achieved for little drag penalty provided that the intake throat Mach number is kept high by elevation of the compression surface For a given total turning of the flow by the compression surface, spillage drag is found to be uniquely related to the inlet mass flow ratio (as distinct from capture mass flow ratio) Radius of the cowl lip is found to affect the drag of the intake at full flow but becomes less important as flow is reduced Drag at full flow for intakes with swept end walls is lower than for a configuration in which they are unswept but the spillage drag rise is greater

(Over)

Cut here

DETACHABLE ABSTRACT CARDS

DETACHABLE ABSTRACT CARDS

At supersonic speeds the variation in full flow drag with compression surface geometry may be predicted from consideration of the changes in shock geometry but there is generally a small positive increment which is not accounted for in the calculation Calculation methods based on theoretical shock geometry are found to over estimate spillage drag

At supersonic speeds the variation in full flow drag with compression surface geometry may be predicted from consideration of the changes in shock geometry but there is generally a small positive increment which is not accounted for in the calculation Calculation methods based on theoretical shock geometry are found to over estimate spillage drag

At supersonic speeds the variation in full flow drag with compression surface geometry may be predicted from consideration of the changes in shock geometry but there is generally a small positive increment which is not accounted for in the calculation. Calculation methods based on theoretical shock geometry are found to over estimate spillage drag

C.P. No. 1269

1974
Published by
HER MAJESTY'S STATIONERY OFFICE

To be purchased from
49 High Holborn, London WC1V 6HB
13a Castle Street, Edinburgh EH2 3AR
41 The Hayes, Cardiff CF1 1JW
Brazennose Street, Manchester M60 8AS
Southey House, Wine Street, Bristol BS1 2BQ
258 Broad Street, Birmingham B1 2HE
80 Chichester Street, Belfast BT1 4JY
or through booksellers

C.P. No. 1269

ISBN 011 470853 3